FACULTY OF MEDICINE AND HEALTH SCIENCES

Phenotypic characterization of induced pluripotent stem cell-derived cardiomyocytes from an arrhythmogenic cardiomyopathy patient carrying a pathogenic variant in desmoplakin

Léa De Bleeckere
Student number: 02103324

Supervisor(s): Prof. Dr. Jolanda Van Hengel, Laurens Léger

Master's thesis presented to obtain the degree of master in Biomedical Sciences
Academic year: 2022 – 202

GHENT UNIVERSITY

Table of Contents

1. Summary 1

2. Layman summary and societal impact 1

3. Introduction 2

3.1 Arrhythmogenic cardiomyopathy 2

3.1.1 Clinical and structural aspects of ACM 2

3.1.2 Genetic basis of ACM 3

3.1.3 Structural components of cardiomyocytes 4

3.1.4 Cardiac action potential 8

3.2 Induced pluripotent stem cells and models for ACM 9

3.2.1 Induced pluripotent stem cell technology 9

3.2.2 3D Engineered heart tissue 11

3.2.3 Current 3D models for ACM 12

4. Materials and methods 15

4.1 hiPSC culturing 15

4.2 Trilineage differentiation 15

4.3 Differentiation and culture of CMs 15

4.4 Immunofluorescence staining 17

4.1.1 Stem cells 17

4.1.2 Cardiomyocytes 17

4.5 Image analysis 18

a. Colocalization of HOECHST and NKX2.5 18

b. Nuclear circularity 18

c. Sarcomere length analysis 18

d. Measurement of fluorescence intensity 19

4.6 RNA extraction and cDNA generation 19

4.7 RT-qPCR 20

4.8 Multi Electrode Array 21

5. Results 22

CRISPR-Cas9 corrected ACM iPSCs maintain their pluripotency 22

ACM iPSCs succesfully differentiate into the three germ layers 22

Differentiation of hiPSC to beating CMs expressing TNNT2 and NKX2.5 22

No significant differences in nuclear circularity between H9, corrected and ACMev10 CMs 26

ACMev10 CMs express a markedly lower Cx43 fluorescence intensity compared to controls 27

Sarcomere lengths in ACMev10 CMs are significantly larger, accompanied by a decrease in α-actinin fluorescence intensity 28

Staining and quantification of plakoglobin reveals nuclear translocation of plakoglobin in ACMev10 CMs 29

MEA analysis shows clustering and higher beating period irregularity in ACMev10 CMs compared to corrected controls 30

6. Discussion 31

7. Conclusion 35

8. References 36

1. Summary

The presence of pathogenic variants in desmoplakin (*DSP*) has been established as one of the main causes of arrhythmogenic cardiomyopathy (ACM), a genetic heart disease. However, little is known about the mechanisms that underlie this pathology with a lack of study on human cells. Due to the delicate position of the heart in the body and to avoid an invasive cardiac biopsy, induced pluripotent stem cell (iPSC) technology has been proposed as an alternative. In this thesis, a closer look is taken at the effects of pathogenic variants in *DSP* in human cardiomyocytes (CMs) derived from hiPSCs. Immunofluorescence staining showed the translocation of plakoglobin from the cellular junction to the nucleus in desmoplakin-mutant CMs derived from hiPSCs. A decrease in fluorescence intensity of plakoglobin and connexin-43 at the cellular border was also noted as well as an increase in sarcomere length and loss of sarcomeric organisation. Overall, *DSP*-mutant CMs present clear phenotypical differences when compared to embryonic and CRISPR-Cas9 corrected controls.

2. Layman summary and societal impact

Arrhythmogenic cardiomyopathy is a genetic disease that affects around 1:1000 to 1:5000 people. Patients with this disease are at higher risk of sudden cardiac death, and sometimes no symptoms appear before it is too late. It affects rather young people in their forties. However, the disease remains largely misunderstood. For this reason, the present thesis tries to shed light on the early mechanisms that occur in the heart and that lead to the development of arrhythmogenic cardiomyopathy. The aim is to get a better understanding of the disease so that, in the future, a targeted therapy becomes available to help the patients, improving their quality of life as well as their life expectancy. The topic is of general interest for the healthcare sector with a focus on patient wellbeing.

3. Introduction

3.1 Arrhythmogenic cardiomyopathy

Arrhythmogenic cardiomyopathy (ACM) is a progressive autosomal dominant disease of the inner cardiac muscle mass and has a prevalence of about 1 in 1000 to 1 in 5000 [1]. Clinically, it is defined by ventricular arrhythmia – either monoventricular or biventricular – potentially leading to sudden cardiac death [2]. Pathophysiologically, ACM is caused by pathogenic variants in genes coding for several structures found in the intercalated disc (ID), a heart-specific junctional structure that allows for cellular adhesion and communication. It is estimated that 60% of pathogenic variants found in ACM patients carrying a mutation are present in desmosomal genes encoding for proteins desmoglein-2 (DSG2), desmoplakin (DSP), plakophilin-2 (PKP2) or plakoglobin (PG) present in the ID. However, other mutations – even though less common – can be causal for the disease as well, such as in proteins found in the area composita of the ID or in nuclear lamin A/C [3, 4]. In about 35%-50% of cases, no genetic abnormalities can be found at all, underlining the very heterogeneous nature of the disease [2].

3.1.1 Clinical and structural aspects of ACM

Early manifestations of ACM include ventricular arrhythmia, myocarditis, tachycardia and cardiac arrest. Symptoms usually arise during the first half of life - around the fourth decade - although the variable and aspecific nature of these symptoms make diagnosis challenging. Symptomatic patients will mostly be alarmed by chest pain and palpitations, leading to a visit to the cardiologist and subsequent diagnosis. However, a subset of patients remains asymptomatic until later in the disease progression, where the damage to the cardiac tissue has already progressed and the patient might have suffered a minor cardiac infarct [1]. In blood analysis, elevated serum troponin levels due to cardiac arrest can be detected, while an electrocardiogram can display changes in the ST-segment as well as abnormal depolarisations [1].

For long, ACM was considered to affect the right ventricle exclusively, with patients being diagnosed having *arrhythmogenic right ventricular cardiomyopathy*. However, recent advances have demonstrated the involvement of the left ventricle as well. It is estimated that 60% of patients suffer from a biventricular phenotype [2, 5]. We thus distinguish right ventricular, left ventricular and biventricular phenotypes, depending on the affected ventricle, which is typically dilated and is the source of the arrhythmias [1, 2]. Biventricular ACM is characterized by an equal involvement of both ventricles, where arrhythmias originate from either ventricle. A biventricular phenotype is correlated with more severe cases of ACM [1]. However, according to Rampazzo and colleagues, involvement of both ventricles is only seen at the end-stage of the disease [3]. Along with the high degree of variation in symptoms linked with ACM, age and biological gender were also found to play a role, with male patients being more at risk [6]. At this moment, ACM is considered to be a disease of the ID, a structure safeguarding the coupling of adjacent cardiomyocytes (CMs) as well as their communication. As will be explained later, the ID consists of several proteins that together form this junctional structure [2, 5].

Repeated cardiac arrests due to unsynchronized depolarisation damages cardiac tissue, resulting in the formation of fibro-fatty scarring tissue as a replacement for lost cardiomyocytes. Typically, this scarring tissue can be found in the affected ventricle [2]. In an advanced stage of the disease, remaining CMs find themselves trapped in a pool of fibro-fatty deposit, increasing the fibrotic load especially in the epicardium [6]. In patients carrying a mutation in *PKP2*, epicardial cells are thought to be the source of this fibro-fatty tissue replacement [7]. Macroscopically, ventricular dilation sometimes leading to aneurysm, and thinning of the

ventricular wall leading to an increased risk of rupture can be observed. When dilation is observed, the diagnosis of ACM with ventricle dilation is used. As reported by *Stevens et al.* in their research using mouse induced pluripotent stem cell (iPSC)-derived CMs carrying a heterozygous mutation in *DSP*, arrhythmias could only be observed after applying pressure overload. Simply put, they described that arrhythmia is not a spontaneous manifestation of ACM. Rather, *DSP* pathogenic variants cause the heart to become more sensitive to mechanical stress. This increased afterload results in ventricular dilation, decreased cardiac function and increased risk of arrythmia [8]. It should be noted that these architectural changes to the cardiac tissue are mostly secondary to ventricular arrhythmia, meaning that electrical defects often occur before structural remodelling can be observed, bringing forth the importance of early diagnosis [1, 8, 9]. Whereas the electrocardiogram is useful in determining first hand abnormalities, imaging methods such as magnetic resonance imaging can be used to observe these structural changes.

3.1.2 Genetic basis of ACM

According to *Smith et al*, about 50% of patients manifesting symptoms of ACM are found to have a genetic mutation in at least one of these desmosomal genes [1, 2]. In adults, pathogenic variants in *PKP2* are most prominent, while in younger patients *DSP* seems to be mutated more frequently [1]. Besides this, men seem to be more affected than women [2].The most prevalent mode of inheritance is autosomal dominant, with low to incomplete degrees of penetrance again pointing to the variable symptoms of the disease [1].

a. Mutation classification in ACM

Mutations such as those found in *DSP* can be classified as truncating or non-truncating mutations. A truncating mutation is defined as a mutation which leads to a truncated (shortened) variant of a protein being translated, leading to allelic loss and reduced expression [6]. A truncated protein is produced when the mutation leads to a premature stop codon, such as in frameshift (the mutation leads to a shift in reading frame), nonsense (a single base pair is mutated and translates to a stop codon) or missense (a single base pair is substituted by another one) mutations [1, 10]. Importantly, missense mutations can be truncating, but are not always: the mutation may also result in a faulty protein, or in a normal protein due to codon redundancy. We therefore decided to use the “truncating” and “non-truncating” nomenclature as opposed to “truncating” vs. “missense” nomenclature, which may lead to confusion. It should be noted that in the case of a truncating mutation, the affected protein may not always be detectable in the patient as the mutant transcript often gets degraded before its translation via nonsense-mediated RNA decay [10].

b. The DSP gene

Within the *DSP* gene located on chromosome 6p24.3 several loci can be found that can carry a pathology-causing mutation (Fig. 1). The N-terminus binds to intracellular PKP2 and PG mediating protein-protein interaction [3]. *Stevens* and colleagues have previously referred to this region as a ‘terminal hotspot for ACM variants’, as it has been shown to be especially sensitive to calpain-mediated decay [8]. A central Rod domain helps in associating with intermediate desmin filaments, a process catalyzed by the C-terminal desmin binding domain. During protein synthesis, DSP undergoes alternative splicing to generate 3 isoforms: DSP1, DSP1a and DSP2. These isoforms differ from each other through their length, mainly attributable to the variable length of the Rod domain [3]. Truncating mutations are found across the gene, while non-truncating missense mutations are principally found in the PKP/PG-binding and desmin-binding units of the gene [10].

Fig. 1: Schematic representation of the functional domains of the *DSP* gene, based on *Rampazzo et al., 2006*. [3]

A recent clinical study comparing a cohort of patients carrying a truncating mutation in *DSP* to a cohort carrying a mutation in *PKP2* has found that left ventricle dominant ACM prevails in cases with *DSP* pathogenic variants [10]. Right ventricle ACM on the other hand was predominant in the *PKP2*-mutated cohort. Moreover, in patients carrying a *DSP* mutation without familial antecedents, left ventricle impairment was shown to be less prevalent than in patients with other family members affected by *DSP*-ACM. However, these non-proband patients expressed chest pain and blood troponin levels similar to patients with antecedents [11]. Furthermore, the role of zygosity cannot be underestimated with patients carrying a homozygous *DSP*-mutation showing combined involvement of both heart tissue and skin, while heterozygous carriers typically show impairment of cardiac tissue with more incomplete penetrance [6]. Patients suffering from a homozygous genotype overall present more severe symptoms with a higher risk of cardiac death while compound heterozygous carriers show early (juvenile) onset of disease with excess formation of adipogenic tissue [12, 13].

In ACM patients carrying pathogenic variants in *DSP*, truncating mutations are the primary cause of disease, although non-truncating mutations can also occur. On the other hand, if *PKP2* is affected, non-truncating missense mutations occur more frequently. Combined with the knowledge on *DSP* and *PKP2* pathogenic variants and the subsequent ventricle affected, we can conclude that *DSP* mutations are primarily truncating mutations leading to left-ventricle dominant ACM, while *PKP2* mutations are primarily missense mutations leading to right-ventricle dominant ACM. It should also be noted that mutations occurring in different regions on the *DSP* gene can cause different clinical profiles [10].

3.1.3 Structural components of cardiomyocytes

a. Macroscopic structure and function of the intercalated disc

Individual cells are coupled to each other via junctional structures that allow for mechanical, electrical and signaling communication [5]. In cardiac tissue, these structures are called the ID, which connect adjacent CMs to each other longitudinally (end-to-end) [2]. The ID is in turn composed of several structures, such as desmosomes, gap junctions, adherens junctions and ion channels [5, 14]. The desmosome is a multiprotein structure connecting the intermediate filaments of neighbouring CMs to each other. On the other hand, gap junctions exist of connexins, from which connexin-43 (Cx43) is most prevalent in cardiac tissue, and are crucial in impulse propagation [14, 15]. Adherens junctions are composed of N-cadherins and armadillo catenins that intimately interact with eachother [5]. These catenins comprise PG, p120 catenin and β-catenin [5]. Playing a role in the Wnt-pathway, β-catenin is a well-studied protein that is bound to the F-actin cytoskeleton [5]. Cadherin-catenin complexes are anchoring sites for myofibrils consisting of sarcomeres, the contractile units of cardiac muscle cells. Additionally, these structures can be co-located in the so-called area composita, a mixed-type junction composed of proteins found in genuine desmosomes and adherens junctions, linked together via αT-catenin [2]. The area composita is estimated to occupy as much as 90% of the total ID area. The remaining space is filled with single desmosomes or gap junctions, while a small fraction of the ID is junction-free [5]. Transmission of an impulse - that in the heart originates in cardiac pacemaker cells - is possible as a result of these macromolecular protein complexes that are linked to intermediate filaments and the actin cytoskeleton [14, 15]. Consequently, disruption of either of these junctional complexes due to mutations may affect

proper impulse signaling and protein interactions in the ID, resulting in arrhythmia, fibrillations and even sudden cardiac death [1-3].

b. The desmosome

The desmosome is one of the specialized junctional structures that can be found in the ID. Acting as a cellular adhesion structure, it maintains the mechanical integrity of cardiac tissue by anchoring intermediate filaments from adjacent cells to sites that are subject to high mechanical load, forming a dense cytoskeletal network [2, 14, 16]. The desmosome is composed of several proteins from which DSP, DSG2, PKP2 and desmocollin-2 (DSC2) are the most prominent [2, 16]. Cadherin family members DSG2 and DSC2 link two adjacent CMs via their extracellular domain. Importantly, the role of calcium ions is crucial for cellular adhesion, by binding the extracellular domains of DSG2 and thereby negatively impacting their flexibility [16]. The extracellular DSG2 and DSC2 domains are linked to armadillo-type proteins PKP2 and PG, which are finally bound to DSP (Fig. 2) [16]. DSP tightly regulates force transmission by binding desmin intermediate filaments found at both ends of the sarcomere (Z-discs), thereby transducing changes in force and tensile strength towards the nucleus [5, 10, 16]. Due to the tight relationship existing between the desmosome and the sarcomere, it could be possible that a deregulated desmosome – for example due to a *DSP* mutation – leads to dysfunctional contractile dynamics [17]. As mentioned before, the adherens junction is bound to F-actin via catenins. The actin cytoskeleton and desmin intermediate filaments thus both act as anchoring sites for respectively adherens junctions and desmosomes [2]. DSP plays a major role as a desmosomal binding protein, and *Smith et al.* have suggested that *DSP* cardiomyopathy is a distinct form of ACM characterized by left ventricle dominance and injury, followed by fibrosis in the same ventricle [10]. Due to the high prevalence of ventricular arrhythmia which can sometimes lead to cardiac death as well as its high degree of penetrance, it is important to gain more insight in *DSP*-related ACM [17].

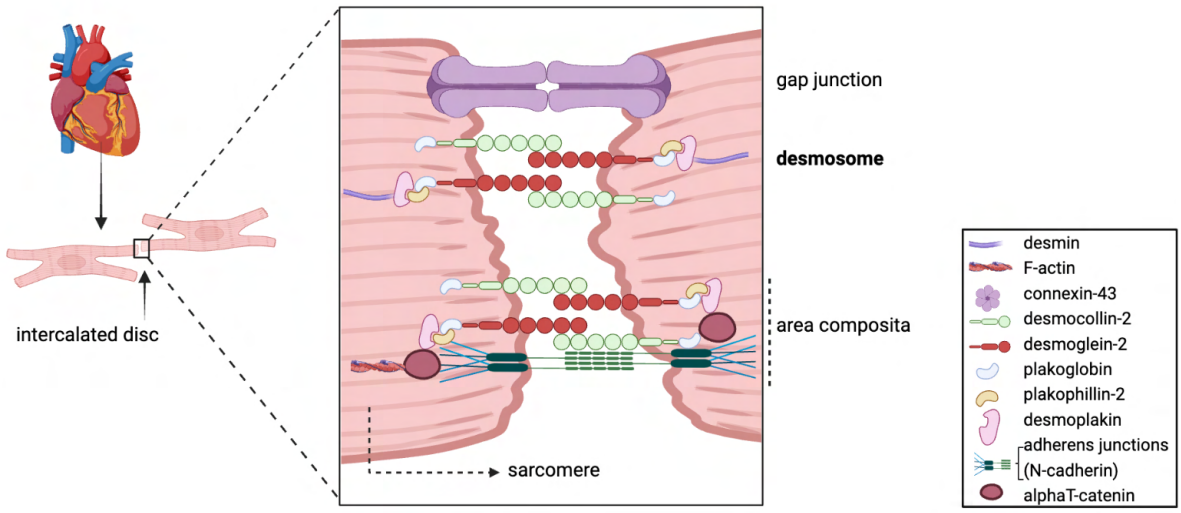

Fig. 2: Schematic presentation of the intercalated disc and its macromolecular protein strucures. DSG2 and DSC2 link two adjacent cardiomyocytes via their extracellular domain, which is bound to intracellular DSP via PKP2 and PG. DSP is bound to the desmin intermediate filament. Figure based on *Rampazzo et al., 2014* [5] & *Austin et al., 2019 [1]*.

Although DSP is situated at the end of the desmosomal protein cascade, mutations in the *DSP*-gene can have a considerable effect on other desmosomal proteins that cannot be underestimated. More specifically, the consequences of *DSP* mutations on PKP2 and PG can reveal more about the mechanism of ACM. PG is known to be a paralogue of β-catenin, a protein important in the canonical Wnt-signaling pathway which regulates cell survival, proliferation and self-renewal capacities of stem cells [18]. β-Catenin serves multiple functions

as junctional protein on the cellular membrane as well as in the regulation of Wnt-ligand-dependent gene transcription [1]. In absence of a Wnt-ligand, β-catenin is degraded cytoplasmically stimulating cellular differentiation ('Wnt-off'). However, when a receptor-ligand interaction occurs, this degradation is inhibited leading to the nuclear translocation and accumulation of β-catenin, in turn inhibiting differentiation and thus promoting the stem cell state ('Wnt-on') [1, 19]. As a β-catenin paralogue, PG inhibits the transcriptional activity of β-catenin while promoting its degradation [19]. In forms of ACM with *DSP* mutation, translocation of PG to the nucleus - probably due to insufficient support of DSP - may cause a 2-fold reduction of Wnt/β-catenin signaling [5, 13]. This has been suggested to increase adipogenesis in mesodermal stem cells, which can be linked to the ventricular fibro-fatty deposits typically seen in ACM patients [5, 13]. In general, nuclear translocation of PG sometimes accompanied by a decreased expression can be seen in human *DSP*-mutant CMs [6, 9].

c. Gap junctions and ion channels

As mentioned previously, gap junction channels are determinant in the propagation of the electrical impulse [14]. Gap junctions in the intercalated disc consist of connexins (Cx45, Cx40 and Cx43), all three occurring in atrial and ventricular myocardial tissue with Cx43 being most abundant in the ventricles [2]. A single gap junction channel assembles through non-covalent binding of two connexons expressed by adjacent CMs, each composed of six connexin units. Depending on the composition of the connexons (homodimer or heterodimer), electrical conductivity differs with homodimers showing larger conductivity compared to heterodimers [2, 14]. Study has shown that connexins work cooperatively, i.e. that a reduction in expression of a connexin in a heterodimer will lead to a compensatory expression of the other connexin present in the dimer [2]. Interestingly, as mentioned by *Gutstein et al.*, a strong decrease in Cx43 (encoded by *GJA1*) has been linked to ventricular arrhythmia in Cx43 knockout mice, with slower impulse propagation and bad CM coupling. This study found that a decreased presence of Cx43 to less than 18% is disease-causing [20]. Furthermore, decreased presence of cardiac sodium-channel protein $Na_V1.5$ (encoded by *SCN5A*) has been linked with ACM in a small number of patients carrying a *SCN5A* missense mutation [1, 14]. $Na_V1.5$ has been shown to co-localize with Cx43 in the ID, suggesting a relation between the two [14]. For example, *Yao et al.* discuss a neonatal rat line knocked out for Cx43 in atrial CMs. A decrease of roughly 50% in Na^+ current was observed following this ablation [21].

Several studies have also investigated the effect of desmosomal protein mutations on Cx43 and $Na_V1.5$, as opposed to mutations in *GJA1* or *SCN5A*. In mice, *Zhang* and colleagues demonstrated how *DSP* silencing markedly reduced the expression of Cx43 and $Na_V1.5$. Moreover, aberrant distribution of both proteins was observed, with Cx43 presence in the intracellular space [22]. The group of *Stevens* created a humanized mouse model carrying a *DSP* pathogenic variant and observed mislocalisation – but no downregulation – of Cx43 [8]. In humans, loss of Cx43 at the ID as well as downregulation was observed in a patient carrying a missense *DSP* mutation [17]. In a recent study, *Van Kampen* and colleagues [15] demonstrated how PITX2, a repressor of Cx43 and $Na_v1.5$, was induced in *DSP*-mutant CMs, further supporting these ideas.

d. The sarcomere

The sarcomere is the contractile unit of striated muscle. Although the sarcomere is not a direct component of the ID, it is in tight relationship with structures found in the ID. Intermediate filaments link the sarcomeres to the cell membrane longitudinally, terminating at the desmosome [17]. It exists of several substructures and proteins and is highly organized. A single sarcomere unit is composed of myosin thick filaments (myofilaments), encoded by myosin light chains 2 and 3, as well as actin thin filaments. Myosin and actin filaments interact with each other directly to yield contraction and are accompanied by troponins (TNNI, TNNT and TNNC) and actinins respectively (Fig. 3) [5, 23, 24]. A sarcomere is defined as the region lying between two Z-bands, forming the edges (Z-discs) of sarcomere units. Within the sarcomere, two types of regions are discerned: The A-band consists of overlapping actin and myosin filaments, while the I-Band does not comprise myosin filaments. The development of such contractile sarcomeric network is crucial to mediate sufficient contraction, which is regarded as an important parameter in determining CM maturity. Therefore, both sarcomere length and alignment are important parameters to ascertain CM maturity [23].

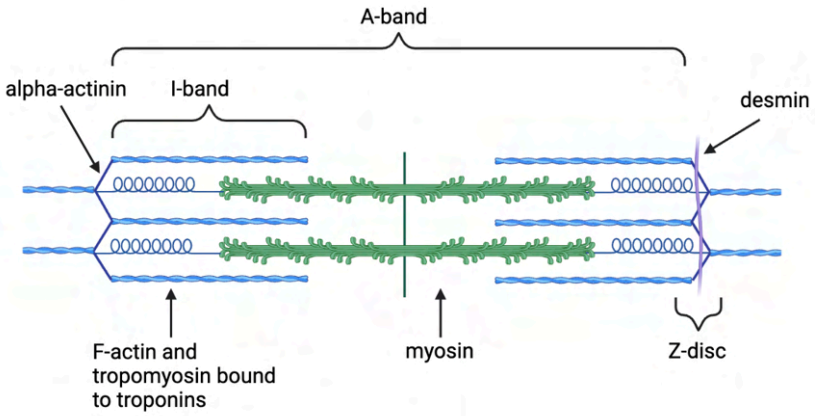

Fig. 3: Schematic representation of the sarcomere and its subunits, based on *Martin et al., 2020.* [24]

Several changes can be observed during the CM maturation process. These changes can be divided into structural and non-structural changes. Accordingly, specific changes in gene expression can be noted. Structural and ultrastructural changes include, aside of increased sarcomere length and organization, the formation of T-tubules, an increased presence of Cx43 at the ID as well as in cardiac *TNNI3*, changes in expression of channels mediating in conductivity (e.g. decreased *HCN4*) and the formation of gap junction channels (e.g. *GJA5*). Non-structural elements associated with the maturation process of CMs are the presence of a metabolic switch to oxidative phosphorylation and increased calcium-handling properties (e.g. *CAV3*) [23, 25].

In healthy cardiac tissue, the average sarcomere length of mature CMs reaches around 2,2 µm, with a high degree of alignment and the formation of an organized sarcomere network [23, 26]. In CMs derived from patients suffering from ACM, however, changes in sarcomere length are yet to be studied. A significant decrease in sarcomere length has been observed by *Wu et al.* in their hiPSC-derived model for hypertrophic cardiomyopathy, with a mean length of 1,78 µm as opposed to 1,99 µm for control CMs [27]. This trend could also be seen in the study conducted by *Wang et al.* for the same condition [28].

e. LaminA/C and the nuclear membrane

Mutations in the gene coding for lamin A/C (LMNA) have been associated with ACM [4]. Lamin A/C are intermediate filament proteins which form an envelope around the nucleus, called the nuclear lamina. Lamins are crucial to safeguard the integrity of the nucleus and to allow for mechanostransduction [4]. In forms of ACM with LMNA mutations, abnormal aggregation of LMNA in the lamina and nucleoplasm were observed [4].

3.1.4 Cardiac action potential

The action potential is an electrical phenomenon where the voltage across the cellular plasma membrane changes polarity. It is absolutely crucial in the functioning of the body, from transmitting information along nerves to allowing for contraction of the heart that provides oxygen for the functioning of other organs [29]. The cardiac action potential differs from potentials found in the brains' neurons or skeletal muscles. For example, the duration of a cardiac action potential lasts about 200ms to 400ms, whilst neural potentials typically are a lot shorter, around 1ms (Fig. 4) [30]. In the heart, the action potential is initiated in sinus node cells, also known as pacemaker cells, and spreads to the atria to cause their contraction. In a next stage, the stimulus reaches the ventricles by passing the atrioventricular node [29]. We thus distinguish pacemaker and non-pacemaker cells. An action potential is initiated when the electrical stimulus surpasses a certain threshold. The membrane then depolarises due to the opening and closing of sodium channels. Importantly, calcium ions are involved in the process as well. In the heart, these calcium ions cause the initial depolarisation of pacemaker cells, while in non-pacemaker cells the calcium ions cause the prolongation of the action potential until it reaches a plateau phase [30]. Such action potentials can be measured in vitro using MEA and can reveal more about potential arrhythmias occuring. An arrhythmia can occur due to prolonged repolarization and impaired conduction of the electrical impulse [29].

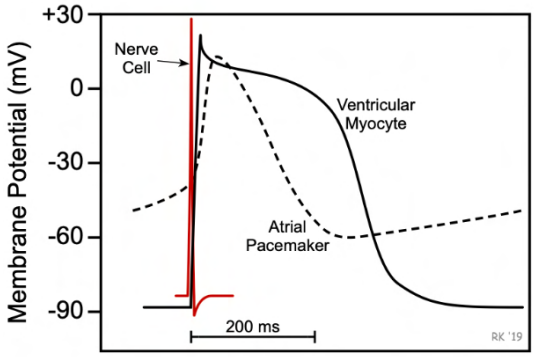

Fig. 4: The cardiac action potential by *Klabunde et al., 2017. [30]*

3.2 Induced pluripotent stem cells and models for ACM

To avoid the difficulty of sampling cardiomyocytes (CMs) in ACM patients through an invasive procedure such as a myocardial biopsy, induced pluripotent stem cell (iPSC) technology can be an interesting candidate to generate patient-specific CMs [31]. To generate iPSCs, somatic cells are collected through a skin biopsy, blood sample or a urine sample which are then reprogrammed to their pluripotent stem cell state using four key transcription factors (OSKM). Delivery of the transcription factors can be achieved using non-integrating Sendai viral particles, resulting in patient-specific stem cells carrying the original mutation [31]. After successfully culturing these stem cells, differentiation towards CMs can be achieved by using the appropriate small molecules. Using this technique, a large amount of CMs can be generated in a relatively short time. They can be cultured in 2D to study disease and for restorative gene therapy, and can be further propagated in 3D to better mimic *in vivo* heart tissue (Fig. 5).

3.2.1 Induced pluripotent stem cell technology

A pluripotent stem cell (PSC) is a precursor cell that has the ability to self-renew and to differentiate into cells from all three germ layers (endoderm, mesoderm and ectoderm) [32, 33]. Human PSC can only be extracted from the inner cell mass of a blastocyst, consequently named embryonic stem cells (ESC). This means that, in the adult body, no PSC source can be exploited to generate differentiated cells, as adult stem cells are multipotent and no longer have the ability to differentiate into all three germ layers [33]. However, the use of ESC from human embryos to generate differentiated cell types raises many ethical concerns. Animal models have been used extensively to gain knowledge on PSC, but discrepancies exist between animal and human cells rendering extrapolation to man difficult, and transplantation even more so [32]. For these reasons, another source of PSC to generate patient-specific cell lines is desirable.

In 2006, *Yamanaka* and colleagues published a groundbreaking paper in which they demonstrated in great detail how, starting from adult or mouse embryonic fibroblasts, they achieved the induction of pluripotent stem cells [33]. This paper has been referred to and used as a starting point for further research since its publication. In their study, *Yamanaka et al* identified four embryonic transcription factors that can be used to reprogram a somatic cell to a pluripotent stem cell, namely Oct3/4, Sox2, Klf4 and c-Myc (OSKM factors) [33]. The genes coding for the transcription factors were delivered via a retroviral vector, thereby inserting the genes into the host genome. Analysis of colony formation, an important characteristic of pluripotent stem cells, showed that withdrawal of either of the four transcription factors lead to non-embryonic-stem-cell (ESC)-like morphologies. Stem cell colonies that were induced through delivery of the four factors were consequently labeled ‘induced pluripotent stem cells’ (iPSC) and showed ESC-like morphology. Further study of pluripotency using RT-PCR and gene expression analysis showed a marked increase in pluripotency-associated genes, although iPSCs were not identical to ESC. Moreover, embryoid body formation and *in vivo* teratoma formation further confirmed the finding that ESC and iPSC are not fully similar [33]. iPSC enable the generation of a large amount of patient-specific PSC, that can be used both for stem cell research and disease modeling, as well as for personalized cell-based therapy [34].

Although this study revolutionized stem cell research, some important hurdles remained. Importantly, low transduction efficiency and a high degree of tumor formation stood in the way of using iPSC to their full potential. These hurdles could be attributed mainly to the oncogenic nature of Klf4 and c-Myc and to the use of an integrating viral vector, increasing the risks of insertional mutagenesis and chromosomal instability [33, 34]. As reported by *Yamanaka et al* one year after their discovery, about 20% of murine offspring derived from germline-competent iPSC developed a tumor due to c-Myc overexpression [34]. To tackle these issues, several

actions have been undertaken in the years following. Firstly, the use of non-integrating viral particles (e.g. Sendai, adenovirus) as opposed to integrating viral particles can avoid the risks of insertional mutagenesis.
Still, by using a viral vector – whether integrating or not – the risks of chromosomal instability remain high as viri damage the plasma membrane when injecting their genome into host cells [33]. Therefore other non-viral delivery methods are available, such as transposons, delivery through mRNA or proteins, plasmids and episomal DNA [34].

Another strategy to improve iPSC efficiency is to replace oncogenes Klf4 and c-Myc by other pluripotency-associated genes. In 2007, Thompson et al modified the OSKM cocktail by substituting Klf4 and c-Myc with Nanog and Lin28 (OSNL factors) respectively and using a lentiviral delivery method [34]. However still, efficiency remained low. Because leaving out either of the four minimal transcription factors would affect pluripotency [33], a better approach seemed to combine the OSKM/OSNL factors with other pluripotency enhancing genes. For example, the combination of OSKM/OSNL with *undifferentiated embryonic cell transcription factor 1* or with *sal-like protein 4* was proved to enhance reprogramming efficiency [34]. Moreover, the use of non-coding RNA's such as miR302 was also shown to increase efficiency. Lastly, a range of small molecules have surfaced that can help achieving this goal [34]. These include for instance ascorbic acid (reduces senescence), trichostatin A (histone deacetylase inhibitor) and pharmacological inhibition of GSK3 using CHIR9902 [34]. Supplying culturing media with small molecules has been proved an effective strategy in enhancing iPSC efficiency.

Patient-specific stem cells can thus be generated without the need of human embryos, bypassing the ethical concerns associated with them as well as immune rejection when transplanting differentiated cells back into the patient (autologous transplant) [32]. Moreover, iPSCs allow for disease modeling and gene editing of PSC derived from patients carrying a genetic disease. Using gene editing tools such as CRISPR-Cas9 it is now possible to replace a mutated gene by its correct copy [32, 34]. In 2021, *Shiba* and colleagues generated iPSC from an ACM-patient carrying a heterozygous *DSG2* mutation [12]. They then sought to correct the impaired *DSG2* allele situated on exon 4 by using CRISPR-Cas9. In order for the Cas9 enzyme to recognize the mutated allele, a guide RNA (gRNA) targeting the specific sequence on exon 4 is necessary. After insertion of the Cas9-gRNA complex into the host cells via electroporation, Cas9 will cut the impaired allele and induce non-homologous end joining. Following this, a repair template was generated containing the correct sequence which inserts itself into genome via homology-directed repair [12]. Naturally, gene editing should not affect the pluripotency of the corrected stem cells. This can be easily checked by looking at gene expression analysis and embryoid body formation as mentioned before.

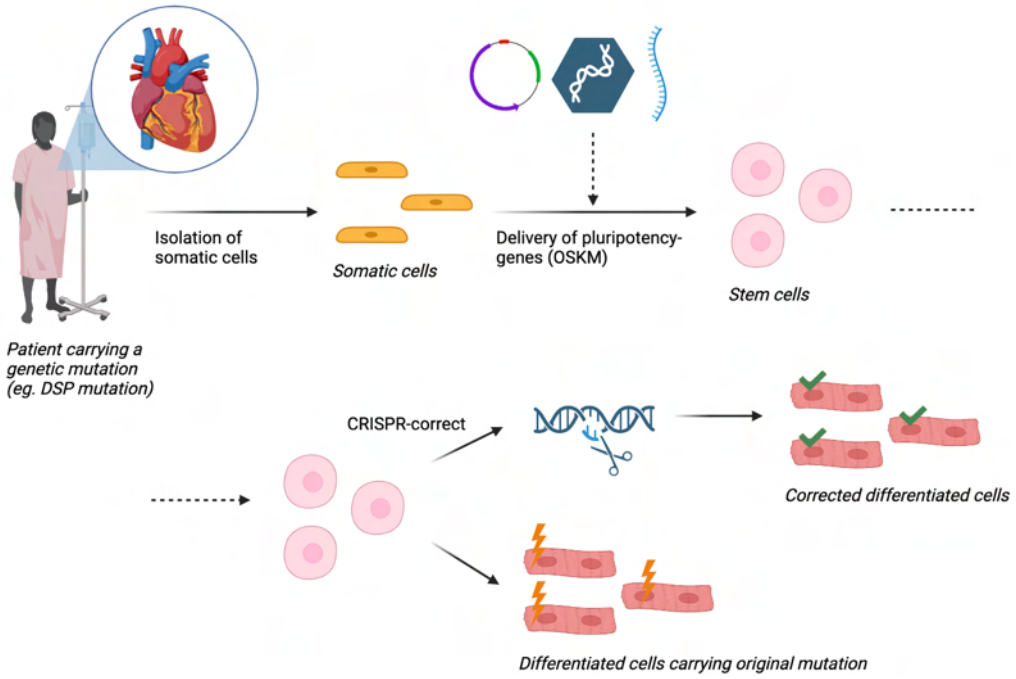

Fig. 5: Induced pluripotent stem cell technology. After isolation of patient somatic cells, these cells can be reprogrammed towards stem cells using viral or non-viral vectors (here: plasmid, virus, mRNA). Stem cells can be differentiated to give rise to progeny still carrying the original mutation, or be corrected using a gene editing tool to such as CRISPR-Cas9 and then differentiated. Based on *Yamanaka et al., 2006 [33]*.

To give a representative image of the data acquired using human biopsy-and hiPSC-derived CMs, we refer to table 1.

Author	Gene	Observation
Borrego et al.* [6] Gomes et al.* [9] Ng et al.* [17] Van Kampen et al. [15]**	*DSP*	Altered distribution and downregulation of Cx43 and PG, and $Na_v1.5$. Decreased expression of desmosomal proteins
Ma et al. [35]**	*PKP2*	Lower *PG* gene expression, no reduction in Cx43 or *DSP*
Inoue et al. [36]**	*PG*	Reduced CM contractility and loss of desmosomal integrity. PG remains localized at the cellular junction while DSG2 and DSC2 detach and diffuse in the cytosol. Cx43 expression levels remain unaffected
Shiba et al. [12]**	*DSG2*	Abnormal localization of PKP2 and PG
Gerull et al.* [37]	*DSC2*	Loss of desmosomal integrity and early ACM

Table 1: Overview of relevant human 2D models carrying a pathogenic variant in desmosomal proteins and their effects. *Models established from human cardiac biopsies. **Models established from human iPSC.

3.2.2 3D Engineered heart tissue

While iPSC in a 2D culture offer a great amount of advantages, they also have their limitations. Mainly, CM immaturity and failure to mimic the three-dimensional *in vivo* environment of the heart remain problematic [32]. Examples of such immaturity include incomplete myofibril alignment, decreased size of individual CMs, lack of T-tubuli and decreased expression of surface ion channels and general lack of structure [32]. Moreover, cells cultured in 2D are more

prone to mutagenesis compared to 3D cultures, meaning cells propagated in a 3D system can be kept in culture mutation-free for a lot longer. Comparative gene expression analysis has demonstrated that CMs cultured in 3D have increased maturity compared to 2D [32]. Presence of T-tubuli can also be observed in 3D systems [32], along with longitudinal orientation, inter-cardiomyocyte coupling and force generation [7, 38]. Additionally, while sarcomeric organization in 2D remains poor, increased organization with a high level of α-actinin can be observed in 3D [39]. Overall, a 3D system offers a more physiological approach to recreating the cellular environment [38]. One such model is called Engineered Heart Tissue (EHT), although other 3D models exist, such as 'heart-on-a-chip' models, the use of scaffold-based approaches or organoids [32].

The question remains of how exactly cells can be propagated from a 2D culture to 3D. Selection of 2D-CMs can be achieved by screening for differentiation efficiency (e.g. *TNNT2* presence with FACS) [7, 39]. Although collagen I has been widely used as a natural coating polymer, a high degree of variability and the need of a large amount of cells has lead researchers to look for an alternative polymer [38]. Fibrin(ogen) is a glycoprotein present in plasma that can be purified from different animal species. Compared to collagen I, fibrin offers a higher elastic modulus resulting in a softer matrix along with a high degree of bio-compatibility. Polymerization of fibrin from fibrinogen leads to gel formation similar to the polymer that is found *in vivo [38]*. For these reasons, fibrin has gained popularity as a scaffold-free approach to 3D culturing. One downside remains its animal origin. CMs mixed with fibin can be casted into agarose molds containing two silicone spots per well [38, 39]. By offering the cells an anchoring point, a preload is generated leading to auxotonic CM contraction against the spots [39]. Auxotonic contraction cannot be seen in 2D cultures and offers muscle bundle formation, increased CM orientation and allignment and increased sarcomere maturity [39].

A 3D system offers ways to bypass aforementioned issues by allowing the cells to grow in space and recreate as closely as possible their natural environment [32, 38]. CMs self-organize within a 3D system. Of course, a multicellular approach containing other cell types present in the heart, such as cardiac fibroblasts, is also possible. To achieve such 3D model, several factors need to be considered: 1) a source of CMs (e.g. iPSC-derived), 2) a scaffold or a low-attachment plate to seed the cells on and 3) the application of external stimuli when necessary [32]. The generation of EHT allows for a plethora of parameters to be tested, such as force and beating frequency as well as contraction and relaxation kinetics [39]. Scaffolds are necessary for cellular adhesion, migration, proliferation and finally differentiation [32]. Primarily, a scaffold should be non-toxic, bio-compatible and porous for adhesion. Its primary aim is to mimic the *in vivo* extracellular matrix (ECM). Several types of scaffolds are available, such as decellularized heart tissue consisting of ECM-proteins or 3D-printed scaffolds. Another strategy is to seed cells on a natural polymer, such as collagen or agarose, or on a synthetic polymer such as polycaprolactone [32, 38]. Scaffolds are however dispensable, as scaffold-free approaches exist such as low-attachment plates or the combination of cells with a material that will solidify (e.g. fibrin) [38]. To reproduce the *in vivo* cardiac environment, application of external stimuli can help increase CM maturity. Such stimuli include electrical (e.g. action potential and voltages) and physical stimuli (e.g. shear stress and hydrostatic pressure) [32]. In their generated EHT, *Hansen et al* increased force generation by applying auxotonic stretch to the CMs, increasing the oxygen supply and supplementing the tissue with insulin [38].

3.2.3 Current 3D models for ACM

In a recent publication (2021) *Shiba* and colleagues demonstrated how they generated so-called three-dimensional self-organized tissue rings (SOTRs, Fig. 6) on which they tested force generation [12]. Using hiPSC-derived CMs from a patient carrying a rare homozygous stop-gain mutation in *DSG2*, SOTRs were generated by seeding CMs in polydimethylsiloxane (PDMS) culture wells with 3 mm pillars central of each well. CMs formed a dense circular

structure around the pillar within a week [12]. Analysis of these structures using Multi Electrode Array (MEA) showed tissue fragility, a decrease in force generation and a reduced conduction velocity. Microscopically, desmosome and intercalated disk disruption were observed. Replacement of one *DSG2* allele using adeno-associated virus as insertion vector showed a restored contraction force [12].

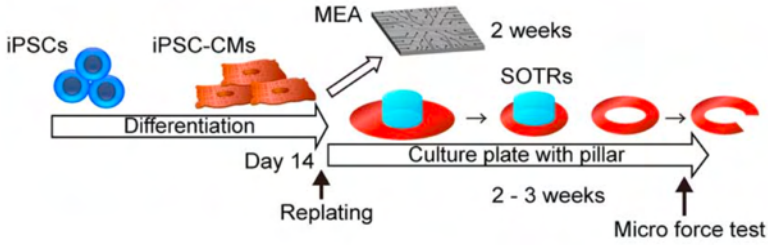

Fig. 6: Generation of self-organized tissue rings (SOTRs) from human induced pluripotent stem cell-derived cardiomyocytes. Picture from *Shiba et al., 2021*. [12]

Prior to this, another study conducted by *Giacomelli* and colleagues presented their scaffold-free microtissues (MTs) (Fig. 7). The MTs were generated starting from hiPSC-derived CMs from a patient carrying a heterozygous mutation in *PKP2* [7]. Importantly, other cardiac cell types were included in this model, namely cardiac fibroblasts (CFs) and cardiac endothelial cells (ECs), making the model multi-cellular. Cell suspensions were created in BPEL medium (5000 cells per 50 μL media) supplemented with adapted growth factors depending on the cell type used [7]. The suspensions were then seeded onto 96-well microplates. Analysis of MTs was performed on day 21. Interestingly, no difference in sarcomere length nor Cx43 expression were observed between controls and ACM-CMs [7]. However, analysis of electrical properties showed a significant reduction in conduction in ACM-MTs at a stimulation above 2Hz with arrhythmic tendencies [7]. A possible cause of this reduced capability to respond to high frequency stimuli may be due to reduced Cx43 expression. This is based on the knowledge that desmosomal proteins mediate Cx43 trafficking, although lowered Cx43 was not observed in this study.

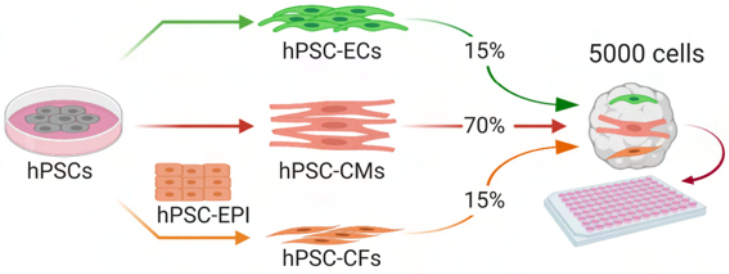

Fig. 7: Multi-cellular microtissues (MTs) used as a model for heart disease. Figure from *Giacomelli et al., 2020*. [7]

The last known 3D model for ACM was presented by *Bliley* and colleagues in 2021 [40]. Together they created an EHT model able to mimic both the preload and afterload of cardiac tissue. Preload is defined as the force needed to stretch the atria during chamber filling (diastole) while afterload is the pressure the heart counteracts to eject blood into the arterial system (systole) [40]. EHTs were fabricated around a PDMS strip. This strip acted as both a mechanical loading platform to seed hiPSC-derived CMs on as well as a tool to measure contractility [40]. To do this, 14-day-old CMs and CFs both derived from hiPSC were mixed with Matrigel and collagen and seeded around PDMS strips which were placed in PDMS wells. Both a control and an ACM model were created, with the ACM model generated from a patient carrying two segregating mutations in the *DSP* gene. As a next step, the EHTs were either kept in an immobilized state by leaving the PDMS strips in the wells during the full culturing period. On the other hand, a dynamic model (dyn-EHT) was established in which the cells

could contract in an unconstrained manner against the strip, generating both a preload and afterload. Lastly, on day 28, the EHTs were removed from the culturing wells and studied based on their ability to generate force and bend the strip (Fig. 8). The ACM-EHT showed significant reduction in overall desmoplakin expression as would be expected. Interestingly, a two-fold decrease in desmocollin-2 was noted in these pathogenic CMs. Localization of DSP was investigated after application of mechanical stretch, with results showing an altered localization of desmoplakin, plakoglobin and plakophillin-2 in ACM-CMs. Notably, total protein and mRNA levels from whole-cells ACM-CMs lysates were not increased after applying mechanical stretch. This finding strongly opposes to the upregulation of all desmosomal genes that was seen in the control model after application of the same mechanical stretch [40]. The results strongly suggest the inability of ACM-CMs to respond to mechanical stretch, further confirming already existing theories supporting this idea. Further findings include the increase in diastolic length in mutant EHTs, lengthening of the EHTs, decrease in contractile shortening and increased diastolic stress compared to controls [40].

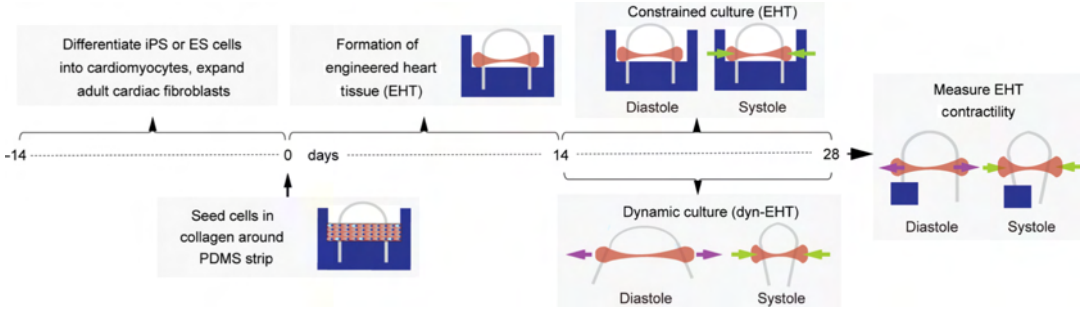

Fig. 8: Generation of strip-format static and dynamic engineered heart tissue models on a collagen & matrigel matrix. Picture from *Bliley et al., 2021*. [40]

4. Materials and methods

4.1 hiPSC culturing

Several protocols have been established for the successful culturing and differentiation of hiPSCs [41], which served as a reference to our own study protocol (Fig. 9). Another approach was tested based on *Maas et al.* [42] with the aim to expand the cell population after differentiation to CMs (Fig. 10).

Stem cells were cultured on 1:100 Geltrex-coated (Life Technologies) plates in E8 medium (E8 basal medium (Life Technologies) with Pen/Strep (Life Technologies) and E8 supplement (Life Technologies)) and kept under hypoxic conditions (37°C, 5% CO_2, 5% O_2). The well-described H9 hESC control, iPSCs carrying the c.817C>T, p.Q273X mutation in *DSP* (exon 7) named ACMev10 and ACMdv4, and lastly corrected isogenic control, were the cell lines employed in this study. Correction for the defect *DSP* gene was performed using the CRISPR-Cas9 genome editing tool. This tool works by providing the cells with the Cas9 endonuclease and a guide RNA to target the defect gene, in this case a single guide RNA specific for the region in which the pathogenic copy in *DSP* resides. A repair template can then be provided which is inserted in the genome by homology-directed repair, whilst the defect gene is cut out. Not all clones used the guide RNA template for correction. Stem cells reprogrammed without repair template will still incorporate the correct allele of the *DSP* gene by homology-directed repair. The stem cells reprogrammed without template were named ACMCORRF1-T, the cells corrected with template ACMCORRF6T. Passaging was done every 3 to 4 days after a confluence of about 80% was reached to allow for further growth. hiPSCs were detached from their well using TrypLE (0,5mL/12 well) (Life Technologies). After incubation, TrypLE was inactivated through dilution with E8 medium. After centrifugation, cells were counted using trypane blue and a Bürker counting chamber. If cells were seeded for differentiation, a concentration of 75 000 cells was used per well and kept in culture in E8 medium supplemented with ROCK-inhibitor: 1:100 RevitaCell (Life Technologies) or 1:1000 Y27632 (ENZO Lifesciences). For regular maintenance of the hiPSCs, cells were replated using a 1:4 to 1:10 ratio, depending on their confluence and the desired time for the next passaging.

4.2 Trilineage differentiation

To confirm the differentiation potential of the patient-derived hiPSC, trilineage differentiation was performed according to the STEMCELL protocol (STEMdiff™ Trilineage Differentiation Kit (STEMCELL Technologies)). For each cell line, one 12-well was tested for differentiation capacity towards endoderm, mesoderm and ectoderm. Additionally, one well of non-differentiated hiPSC was cultured as a control. After passaging, cells were kept in E8 medium for four days. On the day of the start of differentiation when a confluence of about 80-90% was reached, the hiPSC well was detached using 1mL/12 well trypLE and centrifuged for 5 minutes at 200g. The pellet was then washed with PBS 3mL/well and centrifuged for 5 minutes at 300, after which the pellet was put at -80°C for storage. Differentiation of the other 3 wells was initiated using according STEMdiff™ trilineage diffferentiation media. Medium of endodermal and mesodermal cells was refreshed every day during 5 days, while the ectodermal cells were kept in culture and replenished daily for 7 days. Afterwards, cell pellets were collected in the same way as for the hiPSC and stored for further use in RT-qPCR.

4.3 Differentiation and culture of CMs

hiPSC were kept in E8 medium during four days before starting differentiation. A combination of cardio differentiation medium (CDM, RPMI1640 + GlutaMax + HEPES (Life Technologies) with ascorbic acid (Sigma) and albumin (Sigma)) supplemented with small molecules CHIR99021 (Calbiochem) or IWP2 (Calbiochem) was used to guide the cells in differentiation.

CHIR99021 is a GSK3-inhibitor which activates the Wnt-pathway and promotes self-renewal of the cells. On the contrary, IWP2 inhibits the pathway, thereby limiting the self-renewing capacities and promoting the differentiation to CMs (stemcell.com). Mesodermal differentiation was initiated using cardio differentiation medium supplemented with 0,33µL/mL CHIR99021 (day 0). Cells were kept for two days under hypoxic conditions. On day 2, the medium was replaced by CDM supplemented with 1µL/mL IWP2 for two days to guide the cells towards cardiac mesoderm. On day 4, the medium was changed to CDM and replenished every other day for another four days. On day 8 CDM was substituted for cardio culture medium (CCM, RPMI1640 with Pen/Strep and B27 (Life Technologies)). Cells were washed with PBS (Life Technologies) 0,5mL/12-well each time a new type of medium was used. From this day on, cells were kept in CCM medium and refreshed every two days on Mondays, Wednesdays and Fridays. Beating could be observed around day 10, where CMs were transferred to normoxic conditions for further maturation. Around day 14, CMs were dissociated using the Miltenyi Cardiomyocyte Dissociation Kit. To do this, one well per cell line was selected with ideal confluence and morphology, and that showed >90% beating, and washed with PBS. Dissociation solution was prepared using buffer X and 1:10 enzyme T (Miltenyi), from which 400µL/well was used to detach the CMs. A total of around 50 000 CMs per well were replated on 1:10 Geltrex-coated coverslips using replating medium (CCM with FBS 20% (Life Technologies) and Y27632 1:1000).

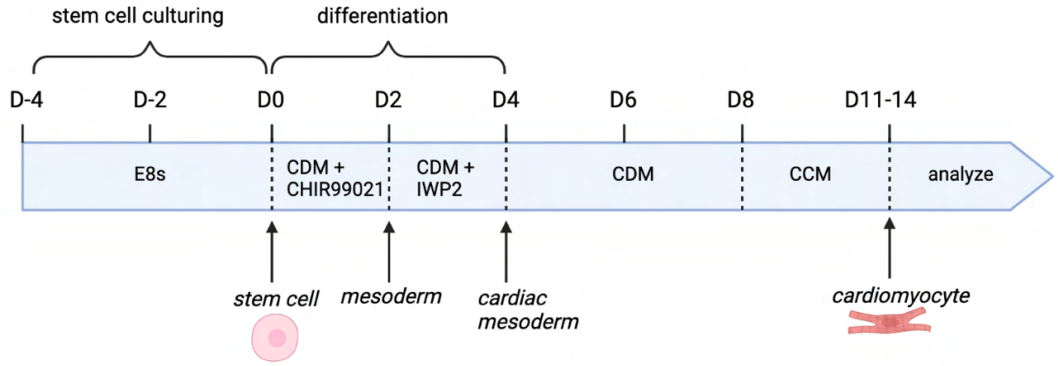

Fig. 9: Schematic representation of the workflow: differentiation of cardiomyocytes from human induced pluripotent stem cells using small molecules. Based on *Burridge et al., 2014*. [41]

To test *Maas* and colleagues' approach, stem cells were maintained in E8s medium for four days before the start of differentiation. On day 0, mesodermal induction was achieved by using 1,5mL/well CDM supplied with CHIR99021. To mimic the embryonic situation better, CHIR99021 levels were lowered through dilution with additional CDM on days 1 and 2. The following day (day 3), further differentiation was initiated by combining a total volume of 1,5mL/well CDM with IWP2. On day 5, the medium was changed to pure CDM after what the cells were maintained in 1,5mL/well CCM. Around day 11 to 14, cells were replated using Miltenyi Dissociation Kit and inactivated using replating medium. To allow comparative analysis, both H9 and ACMev10 cells generated with this protocol and our own were replated. To initiate CM expansion after allowing a recovery of 24h, cardio expansion medium (CCM with CHIR99021 0,165µL/mL) was used at 1,5mL/well volume. Cardio expansion medium was refreshed every two days for a total of three times. CMs were then passaged using cardio splitting medium (CCM with CHIR99021 0,165µL/mL, FBS 20% and Y27632 1:1000).

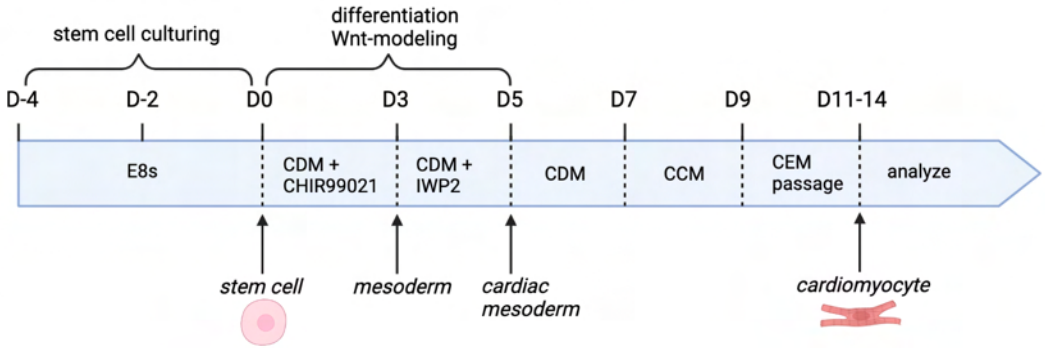

Fig. 10: Schematic representation of the workflow: differentiation of cardiomyocytes from human induced pluripotent stem cells using small molecules. Based on *Maas et al., 2021.* [42]

4.4 Immunofluorescence staining

4.1.1 Stem cells

Cells were washed 3 times for 5 minutes using PBS and fixated during 20 minutes using paraformaldehyde diluted in PBS (4%). A representative table for all antibody dilution factors is shown below (Table 2).

For pluripotency staining of stem cells, blocking solution was made using PBS and 5% goat serum (Life Technologies). Primary antibodies were diluted in a stock dilution solution consisting of PBS, 1% BSA (Merck) and 0,05% Tween20. A total of 2 OCT3/4 antibodies were tested (MCB OCT3/4 A140 and MCB OCT3/4). Double stainings were performed using either SOX2 or NANOG combined with OCT3/4. Staining was performed using a humid chamber and stem cells seeded on coverslips. After overnight incubation at 4°C, the coverslips were washed with PBS and stained with secondary antibody. Secondary antibodies used were goat-anti-mouse 488 and goat-anti-rabbit 594. HOECHST33342 labelling was performed to visualize the nuclei. Coverslips were brought onto microscopy glasses and covered with a droplet of Dabco embedding solution.

4.1.2 Cardiomyocytes

For staining of CMs, fixation was performed around day 30 after a more mature phenotype was reached. 1mL/well permeabilization buffer was prepared using PBS and 0,1% Triton x-100. Blocking solution was made using PBS with 1% bovine serum albumin and 0,05% Tween 20. Antibodies were diluted in blocking solution. Primary antibodies used were troponin-T2 (TNNT2), α-actinin, NKX2.5, lamin A/C, connexin-43 (Cx43) and plakoglobin. All CMs were stained with antibodies for either TNNT2 or α-actinin to validate their CM identity and integrity. Staining using CMs seeded on coverslips and visualization were performed as described above.

Antibody	Dilution Factor	Catalog Number	Firm
OCT3/4 MCB A140	1:200	SC365509	Sigma-Aldrich
OCT3/4 MCB	1:250	O8389-100UG	Sigma-Aldrich
SOX2	1:600	PA1094	Life Technologies
NANOG	1:800	PA1097X	Life Technologies
HOECHST33342	1:1000	H3570	Thermo Fisher
TNNT2	1:250	MA5-12960	Life Technologies
α-actinin	1:800	551353	Sigma-Aldrich
NKX2.5	1:100	701622	Life Technologies
Lamin A/C	1:250	Ab108595	Abcam
Cx43	1:4000	C6219	Sigma-Aldrich
Plakoglobin	1:400	2308	Cell Signaling
Goat-anti-mouse 488	1:500	35553	Life Technologies
Goat-anti-rabbit 584	1:500	35561	Life Technologies

Table 2: Used antibodies, dilution factors and catalog numbers.

4.5 Image analysis

Imaging of stained coverslips was performed using the EVOS FL fluorescent microscope (pictures ware taken on GFP, TexasRed and DAPI channels) as well as the Zeiss LSM900 confocal microscope which uses the ZEN software. For the sole purpose of visualization, brightness and contrast of different channels were adapted using ImageJ. Analysis of fluorescent signals was performed using the ImageJ as well, but on unedited pictures. Methodology was based on reference studies using the same ImageJ tools [23, 25].

4.5.1 Colocalization of HOECHST and NKX2.5

To determine the success of our differentiation protocol, the percentage overlap between blue (HOECHST) and red (NKX2.5) channels was analyzed on TNNT2 and NKX2.5 stained CMs. In ImageJ, a merged image was created and the image type was changed to RGB. The *color threshold* was adapted to include the peaks in hue only. Using the *measure* tool, a measure was then made of those colocalized regions. To calculate a percentage, a ratio was made of colocalized signal against the whole image.

4.5.2 Nuclear circularity

H9, ACMev10 and corrected CMs were subjected to nuclear staining for HOECHST in some cases combined with lamin A/C. HOECHST and lamin A/C stainings were separately analyzed to assess nuclei and nuclear envelope circularity, respectively. Circularity was determined using ImageJ's *analyze particles* tool. Images were converted to 8-bits and the threshold was adapted as little as possible. Parameters such as inclusion of holes and exclusion of image edges were applied. In the *set measurement* section, parameters *centroid*, *fit ellipse*, *area* and *shape descriptors* were enabled. The tool *analyze particles* was then used to calculate circularity. The obtained data was plotted with RawGraphs2.0 and statistical significance was calculated using GraphPad's student's T-test tool.

4.5.3 Sarcomere length analysis

Visualization of the sarcomeres was achieved by staining the CMs for α-actinin. Pictures were taken using both an immunofluorescence microscope and confocal imaging. Sarcomere lengths were determined on confocal images of α-actinin-stained CMs using ImageJ. Images were imported in the program and channels were splitted to avoid interferences with other

fluorescent signals. Using the *straight freehand tool*, a line was drawn perpendicularly across regions of interest (Fig. 11). Under the tool *analyze*, the option *plot profiles* was selected to generate a graph displaying peaks of fluorescence intensity. Lengths were then measured as distance between two intensity peaks, assuming that regions with the highest intensity are the center of the sarcomere. Graphs of the obtained data were made using RawGraphs 2.0 and statistical significance was calculated using GraphPad's student's T-test tool.

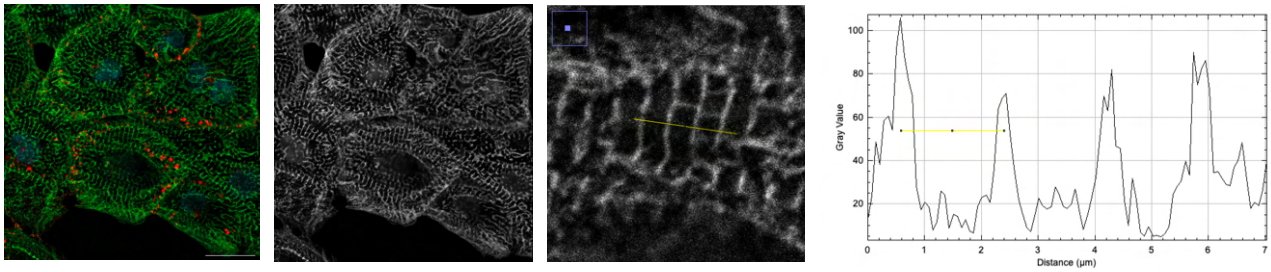

Fig. 11: Sarcomere length measurement using ImageJ in chronological order.

4.5.4 Measurement of fluorescence intensity

Mean fluorescence intensity was analyzed on unedited pictures (no changes to brightness or contrast) taken with the EVOS fluorescent microscopy using ImageJ. Using the *square freehand tool*, a region of interest of same size was selected to cancel out area-related bias. For each analyzed picture, a total of 5 background intensity measurements was taken. The mean background intensity was subtracted from the mean of measured regions of interest (intensity = mean intensity of fluorescent signal – mean background intensity). Measurements were set on *mean gray value*, *area*, *min and max mean gray value* and *integrated density*. Under the tool *analyze*, the option *measure* was selected, yielding fluorescence intensity (density). Graphs of the obtained data were made using RawGraphs 2.0 and statistical significance was calculated using GraphPad's student' T-test tool.

For Cx43 fluorescence analysis, this method proved to be inadequate, yielding divergent results with high standard deviations. For this reason, the approach was slightly modified. Pictures taken on the TexasRed (Cx43) and DAPI (HOECHST) channels were imported into ImageJ. The TexasRed image was used to calculate the total area using the *color threshold* tool. This area was then normalized against the number of nuclei.

4.6 RNA extraction and cDNA generation

Used materials were the GenElute Mamalian total RNA miniprep kit (Sigma-Aldrich) and an On-column DNAse/digestion kit (Sigma-Aldrich). DNAse and DNAse solution buffer were thawed on ice. All used materials as well as the work surface were rendered DNAse-free using ethanol 70% and RNA-se free using NaOH. Lysis solution was prepared using the lysis buffer and 1% β-mercaptoethanol. After incubation with lysis solution (400µL/pellet), the suspension was filtered using GenElute Filtration Column and centrifuged at maximum speed (14 000rpm) for 2 minutes. Next, 250µL of ethanol 70% was added to the filtered suspension. The suspension was then brought onto GenElute Binding Columns and centrifuged at maximum speed for 30 seconds. The flow-through was discarded after centrifugation. A volume of 250µL of washing buffer 1 was added to each column and centrifuged at maximum speed for 30 seconds. After discarding the flow-through, 80µL of DNAse solution was added containing 70µL DNAse solution buffer and 10µL DNAse. After an incubation period of 15 minutes at room temperature, 250µL washing buffer 1 was added to each column. The tubes were centrifuged again at maximum speed for 30 seconds and the flow-through was discarded. 500µL of washing buffer 2 was added to each column. The tubes were centrifuged at maximum speed

during 30 seconds and the flow-through was discarded. This step was repeated once more with a centrifugation of 2 minutes. The tubes were centrifuged one last time at maximum speed for 1 minute. The binding columns were then brought onto new collection tubes and 25µL elution solution was added to each column. The tubes were centrifuged at maximum speed for 1 minute. The collected RNA was stored at -80°C and afterwards thawed for further processing. Sample concentration was measured using the NanoDrop spectrophotometer. Ultrapure water was used to calibrate the instrument and the elution solution served as blank. Parameters that were taken note of were the concentration (ng/µL) and the 260/280 and 260/230 wavelengths.

For cDNA preparation, the biotechrabbit™ cDNA Synthesis Kit (Thermo Fisher) was used. The enzyme and buffer solution were thawed on ice and a Mastermix was created with the following components (amounts per sample): 2µL dNTP mix; 0,5µL RNase Inhibitor; 0,5µL Oligo (dT); 1µL Hexamer Primer; 4µL 5x cDNA Synthesis buffer; 1µL RevertUP™ II Reverse Transcriptase enzyme. A total amount of 9µL Mastermix was used per pellet. The total volume of a PCR tube being 20µL, a maximum of 11µL of genetic material could be added to each one starting with 1µg RNA. In samples where the concentration was too low, the maximal volume of 11µL was used and 9 µL Mastermix was added to reach 20µL. In samples with higher concentrations, the used volume was calculated using the sample concentrations measured with NanoDrop as to use 1µg material. The resting volume was complemented to 20µL using ultrapure water.

$$x\mu\text{L total RNA} = \frac{1000\ ng}{RNA\ concentration\ (\frac{ng}{\mu L})}$$

The material was then stored at -80°C until further use.

4.7 RT-qPCR

We used the Platinum SYBR Green qPCR supermix-UDG (Invitrogen) for real-time PCR. Genes analyzed were *PAX6* and *SOX1* (ectoderm), *brachyury* and *HAND1* (mesoderm) as well as *SOX17* and *FOX2A* (endoderm). Reference genes targeted were *B2M* and *RPL13A*. For the hiPSC, expression of all aforementioned genes was measured to obtain a baseline. Sample Cq values were normalized against this hiPSC expression. For each primer pair, one negative control was included.

All cDNA samples were diluted to 2 ng/µL. A stock solution was created containing the following components, for each primer pair: (10µL SYBR Green, 3,4µL DEPC water, 0,8µL forward primer, 0,8µL reverse primer) *2+2+18% to respectively account for duplicates, negative controls and an error marge. Per well of the 96-well plate, a volume of 15µL stock solution was added as well as 5µL cDNA solution (2ng/µL) or 5µL PCR Grade Water for the negative controls. The plate was then sealed and centrifuged for 5 minutes at maximum speed (350G) after which it was placed inside the CFX96™ Real-Time PCR Detection System. The standard protocol for RT-qPCR was then followed, with the following steps (*repeated 40 times):

2 minutes at 50°C
2 minutes at 95°C
20 seconds at 95°C*
45 seconds at 60°C*
15 seconds at 95°C
5 seconds at 60°C

The obtained data was uploaded into the Bio-Rad CFX manager software and used for further analysis. To calculate the relative gene expression of the target genes normalized to the reference genes, the following formulas were used:

$$\Delta Cq = Cq_{target} - Cq_{reference}$$

$$\text{Average } \Delta Cq_{control\ (iPSC)}$$

$$\Delta\Delta Cq = \text{sample } \Delta Cq - \text{average } \Delta Cq_{control}$$

$$2^{-\Delta\Delta Cq}$$

$$\text{Average } 2^{-\Delta\Delta Cq}$$

4.8 Multi Electrode Array

31 days old CMs were generated and dissociated according to paragraph 2.1. A total of 30 000 CMs were seeded in 8µL Geltrex 1:100 droplets on a MEA plate (Axion Biosystems) and kept in culture with CCM. Recordings were made using the Axion Biosysems Maestro Edge.

Several parameters were looked at, including beat period irregularity, beat period mean, spike slope mean and finally spike amplitude mean. The beat period is defined as the time between two consecutive spikes. The beat period irregularity was calculated using the following formula and gives an indication on the consistency of beatings in time:

$$beat\ period\ irregularity\ (\%) = \left(\frac{standard\ deviation}{mean}\right) * 100$$

The spike slope is defined as the voltage measured divided by the time in seconds, while the contraction amplitude is a measurement of voltage alone and gives an indication on the strength of the contraction.

5. Results

CRISPR-Cas9 corrected ACM iPSCs maintain their pluripotency

For accurate disease modeling, the iPSC lines need to be reliable. Therefore, pluripotency of these lines need to be thoroughly investigated. To this aim, we performed immunostainings for SOX2, NANOG and OCT3/4 in the CRISPR-Cas9 corrected cell lines. The CRISPR-Cas9 corrected stem cells maintained their pluripotency and were tested positive for SOX2, NANOG and OCT3/4 (Fig. 12). Both cells corrected without (ACMCORRF1-T) and with template (ACMCORRF6T) were stained. All three genes are markers for pluripotency and are crucial for maintaining self-renewal capacities. They are expressed in undifferentiated cells (stem cells) and, consequently, their expression gets downregulated in differentiated cells. SOX2, OCT3/4 and NANOG work coöperatively to regulate the transcriptional activity of other pluripotency-associated genes [43].

ACMd and ACMev10 iPSCs succesfully differentiate into the three germ layers

To confirm their pluripotency, differentiation capability to the three germ layers needs to be demonstrated. The ACMdv4 iPSC line carrying the pathogenic variantin *DSP* and the CRISPR-Cas9 ACMCORRF6T cells successfully differentiated into ectodermal, mesodermal and endodermal cells. Ectodermal cells presented a small, round phenotype, while mesodermal cells were flatter and more spread out. The endodermal population showed a tightly packed cuboid morphology (Fig. 13A).
Gene expression analysis using RT-qPCR demonstrated that the differentiated cells expressed more germ layer-specific markers than the iPSCs. Fold changes of germ-layer specific genes were markedly lower in ACMdv4 cells when compared to corrected controls (Fig. 13B). The fold changes were however comparable to the iPSC line ACMev10 (Léger L., manuscript in preparation). All of the tested genes play a major role in cell development. FOX2A promotes the euchromatin state, making DNA more accessible to FOX2A transcription factors and is stably expressed in endodermal tissue [44]. SOX17 is a determinant in endodermal cell fate and activates crucial endodermal genes [45]. On the other hand, brachyury is responsible for the formation of the mesoderm and notochord [46], while HAND1 is important in the formation of mesodermal extraembryonic tissue and cardiac development [47]. PAX6 is crucial in ectodermal neural development and overall neurogenensis [48], along with SOX1 which is one of the earliest transcription factors to be expressed in embryonic development [49].

Differentiation of hiPSC to beating CMs expressing TNNT2 and NKX2.5

Several densities were tested when passaging with the aim to differentiate the cells. From the tested densities – ranging from 50 000 to 125 000 CMs per well – a population of 75 000 CMs was deemed optimal with a confluence of 80-90%. Beating of the hiPSC-CMs could be observed starting day 10 to 14, and were generated from healthy H9 and corrected controls, as well as for the *DSP*-mutant ACMev10 line. Stem cells were successfully cultured and differentiated towards beating CMs using the modified protocol of *Burridge* and colleagues (Fig. 14A). To obtain large quantities of differentiated CMs in a cost-effective way, we employed the protocol of *Maas* and colleagues to expand CMs. This however did not prove successful, with the apparition of aberrant morphology in ACMev10 cells (Fig. 14B).

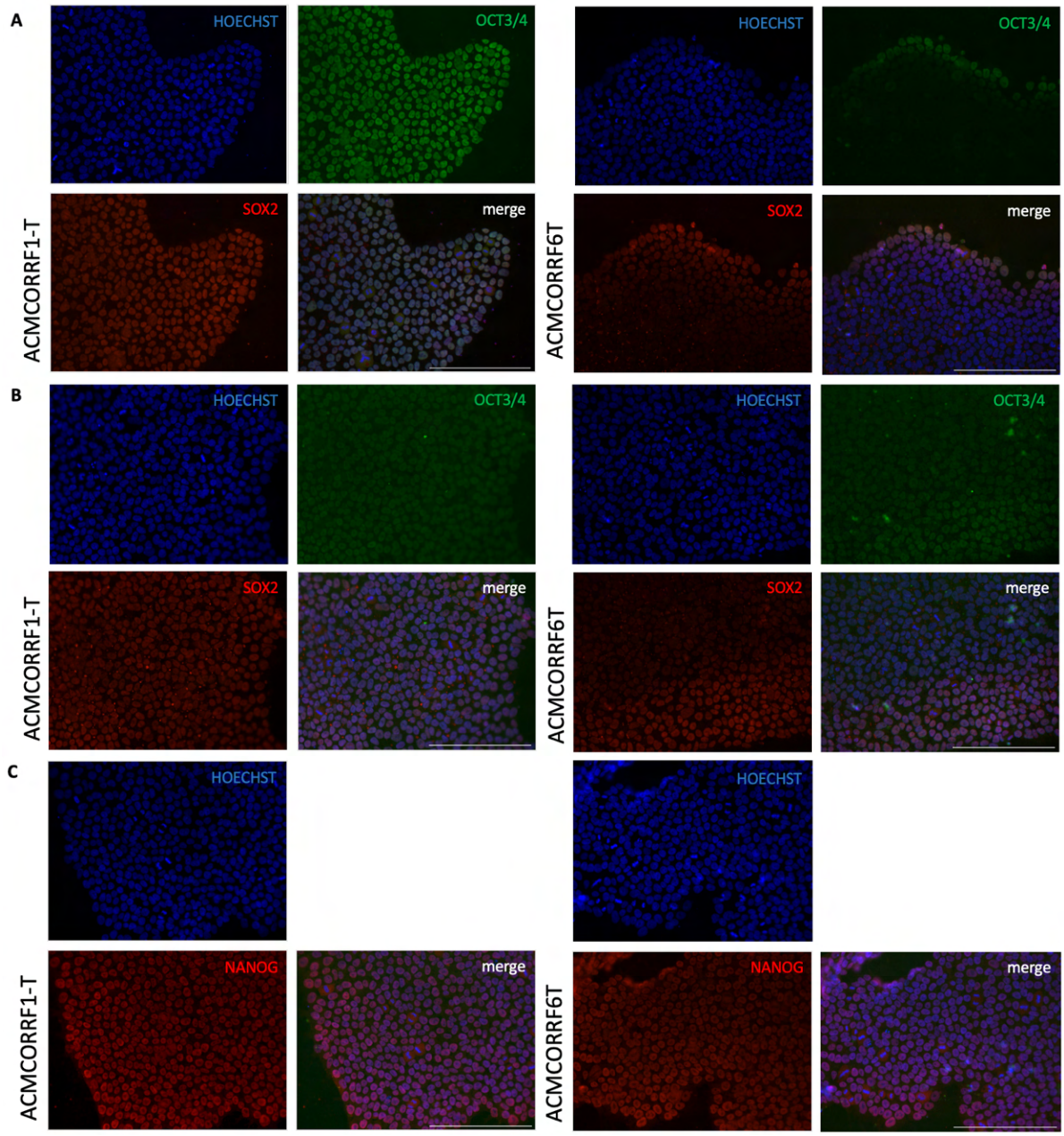

Fig. 12: CRISPR-Cas9 corrected ACM stem cells maintain their pluripotency. Immunofluorescence images of stem cells corrected without (ACMCORRF1-T) or with template (ACMCORRF6T). **A:** Antibodies used were SOX2 and OCT3/4 MCB A140. Scalebar 200µm. **B:** Antibodies used were SOX2 and OCT3/4 MCB. Scalebar 200µm. **C:** Antibody used was NANOG. Scalebar 200µm.

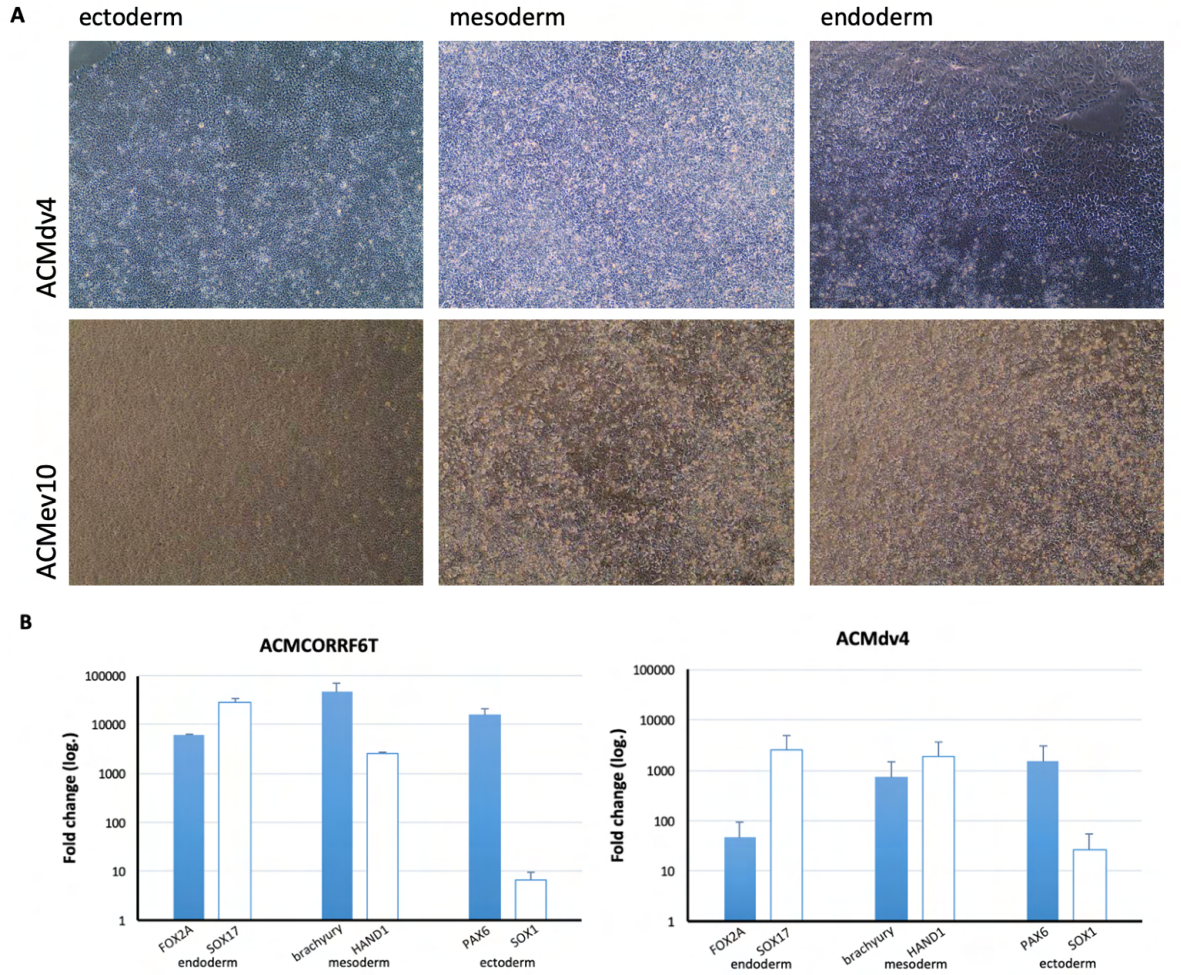

Fig. 13: *DSP*-mutant human induced pluripotent stem cells (ACMdv4) and CRISPR-corrected controls maintain their ability to differentiate into ectoderm, mesoderm and endoderm. **A:** Phase-contrast microscopy images of ACMdv4 and ACMev10 ectodermal, mesodermal and endodermal cells (10x objective). **B:** Fold change of trilineage differentiation-related genes in ACMCORRF6T and ACMdv4 cells compared to induced pluripotent stem cells (logarithmic scale).

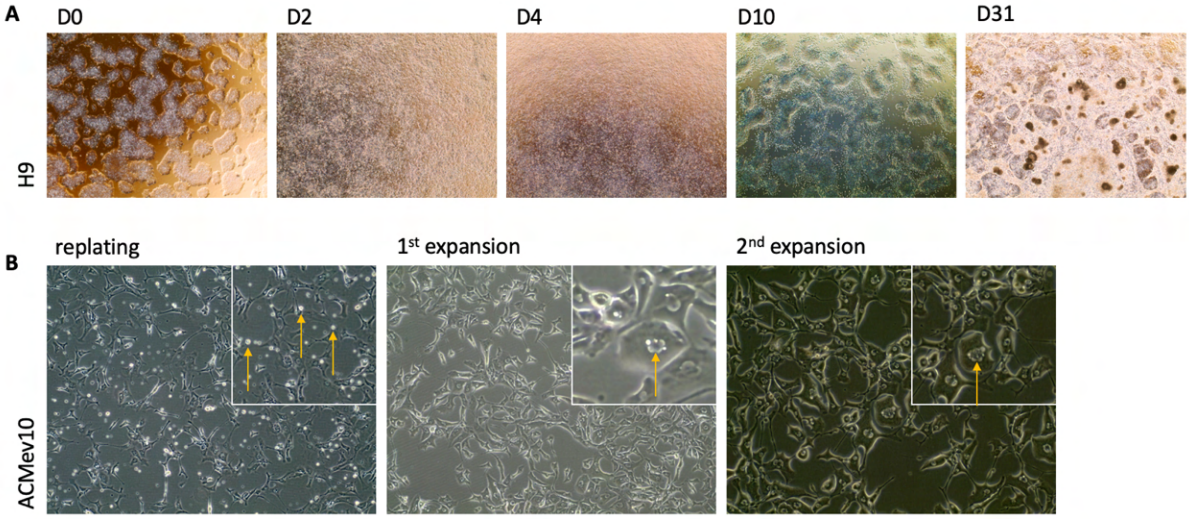

Fig. 14: **A:** Culturing and cardiac differentiation of H9 cells according to the modified protocol by *Burridge* et al. [41] from day 0 (left) to day 31 (right). **B:** ACMev10 cardiomyocytes yielded with the expansion protocol by *Maas et al.* [42] showed abberant morphology and multinucleation.

Differentiation from hiPSC to CMs was further confirmed with fluorescence staining for CM-specific markers TNNT2 and NKX2.5, a CM-specific transcription factor. All embryonic (H9), ACMev10 and corrected (ACMCORRF6T) cell lines were positive for these markers indiciating an efficient differentiation (Fig. 15A). Analysis of differentiation efficacity also showed a high (>80%) overlap between HOECHST and NKX2.5-stained nuclei suggesting an efficient differentiation (Fig. 15B).

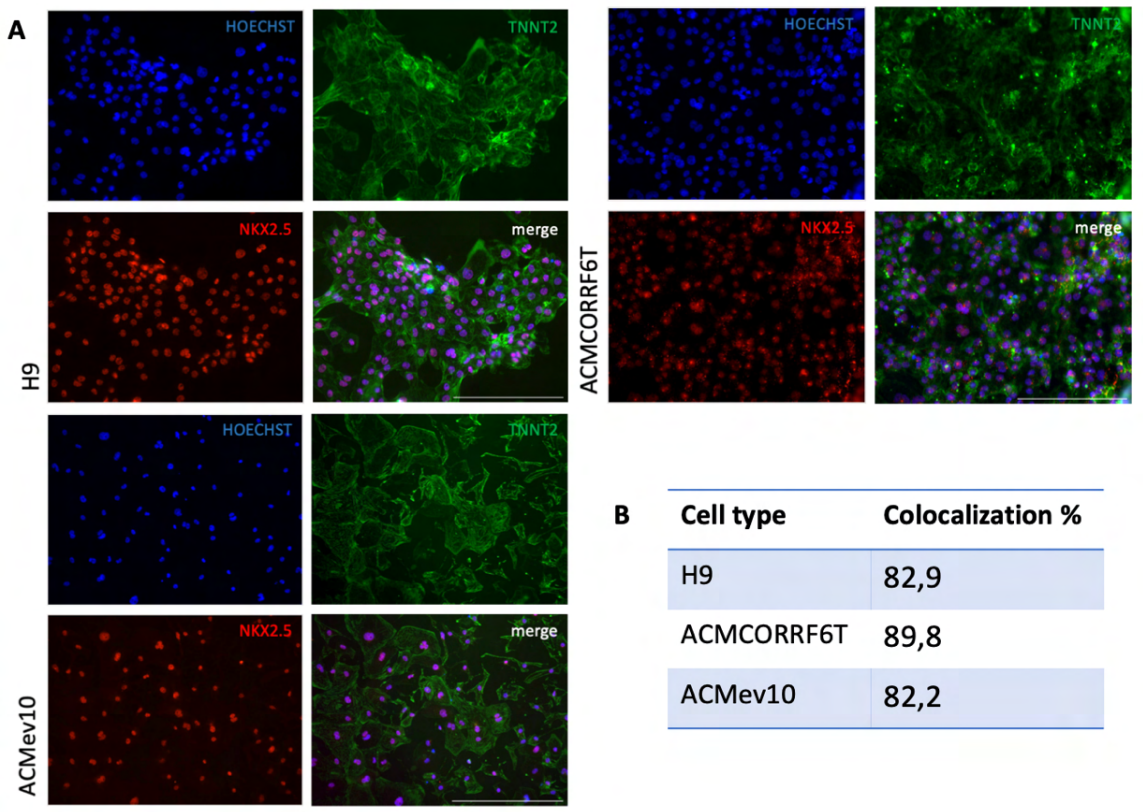

B

Cell type	Colocalization %
H9	82,9
ACMCORRF6T	89,8
ACMev10	82,2

Fig. 15: Successful differentiation of induced plruipotent stem cells to cardiomyocytes expressing TNNT2 and NKX2.5. **A:** Immunofluorescence staining images of 31 days old H9, ACMCORRF6T and ACMev10 cardiomyocytes. Scalebar 200 µm. **B:** Mean overlap of HOECHST and NKX2.5 fluorescent signals in % measured on 3 images per cell line.

No significant differences in nuclear circularity between CRISPR-Cas9 corrected, H9 embryonic or ACMev10 CMs

Fluorescence imaging of α-actinin, HOECHST and lamin A/C-stained CMs showed abnormalities of the nuclear lamina in some nuclei across cell lines (Fig. 16A). For analysis, lamin A/C and non-lamin A/C (HOECHST) stainings were kept separated to investigate the possible influence of lamin on nuclear circularity. The unpaired T-test revealed a significant difference between the circularities of the different CMs (*P*>0,0001*), measured on HOECHST-stained nuclei (Fig. 16B). Analysis of circularity of lamin A/C-stained nuclei revealed no difference in circularities between H9, corrected and ACMev10 CMs (*P*>0,05) (Fig. 16B).

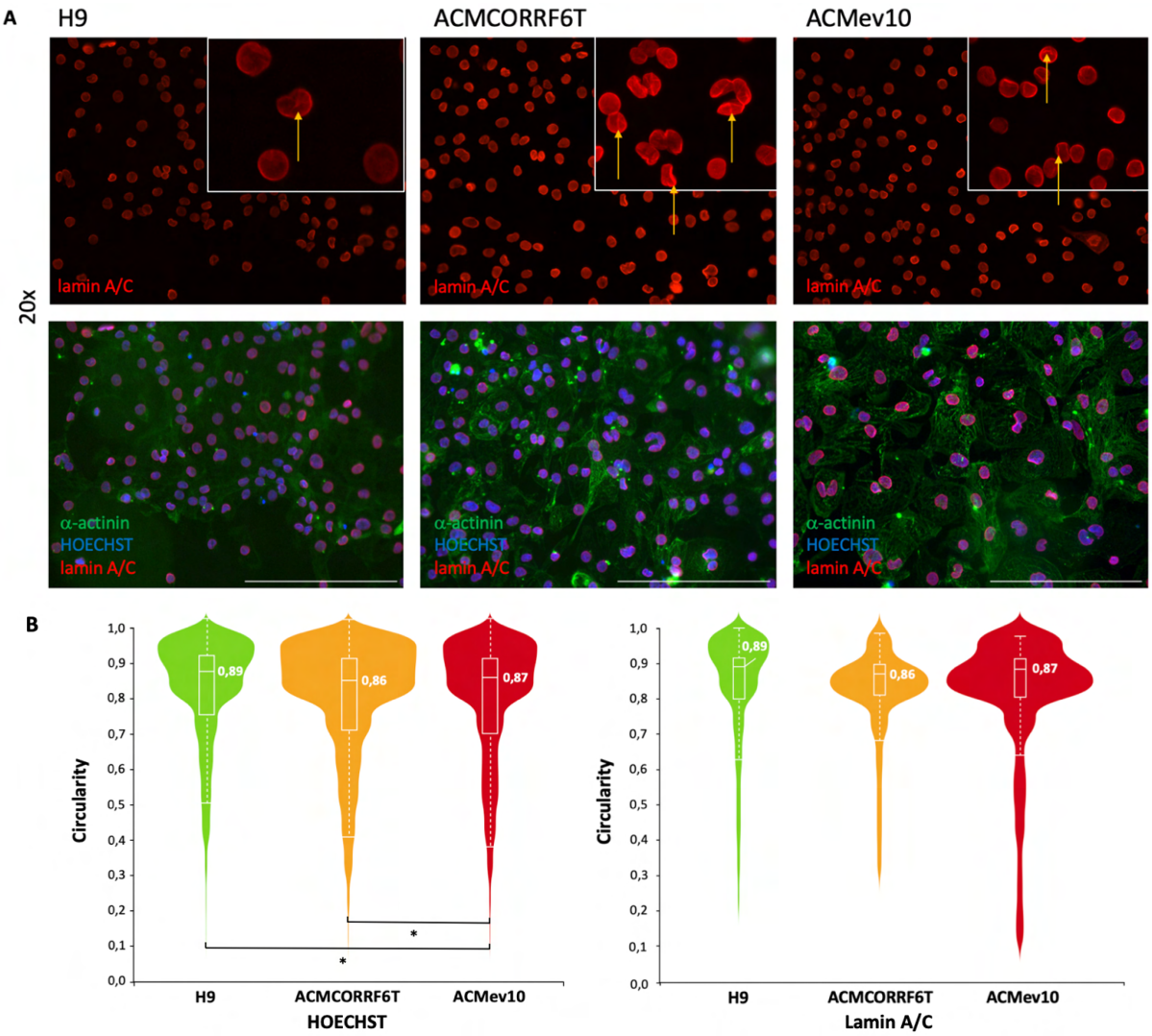

Fig. 16: **A:** Immunofluorescence images of 31 days old H9, ACMCORRF6T and ACMev10 cardiomyocytes stained for α-actinin and lamin A/C. Scalebar 200 µm. **B:** Analysis of nuclear circularity of induced pluripotent stem cell-derived H9, corrected and ACMev10 cardiomyocytes (*P*>0,0001*) (N_{H9} = 1468; $N_{ACMCORRF6T}$ = 1660; $N_{ACMev10}$ = 2460 for HOECHST analysis, N_{H9} = 187; $N_{ACMCORRF6T}$ = 237; $N_{ACMev10}$ = 451 for lamin A/C analysis).

ACMev10 CMs express a markedly lower Cx43 fluorescence intensity compared to CRISPR-Cas9 corrected and H9 embryonic controls

Cx43 expression was confirmed through immunofluorescence microscopy (Fig. 17A). Fluorescence intensities were highest in H9 CMs and lowest in ACMev10 CMs. According to the student's T-test, an extremely statistically significant difference was noted between 31 days old ACMev10 and H9 CMs, and a significant difference was found between 31 days old ACMev10 and corrected CMs (Fig. 17B). Sadly, due to only having yielded one biological replicate for 60 day old cells, it was not possible to calculate a standard deviation for these measurements and thus no T-test could be performed.

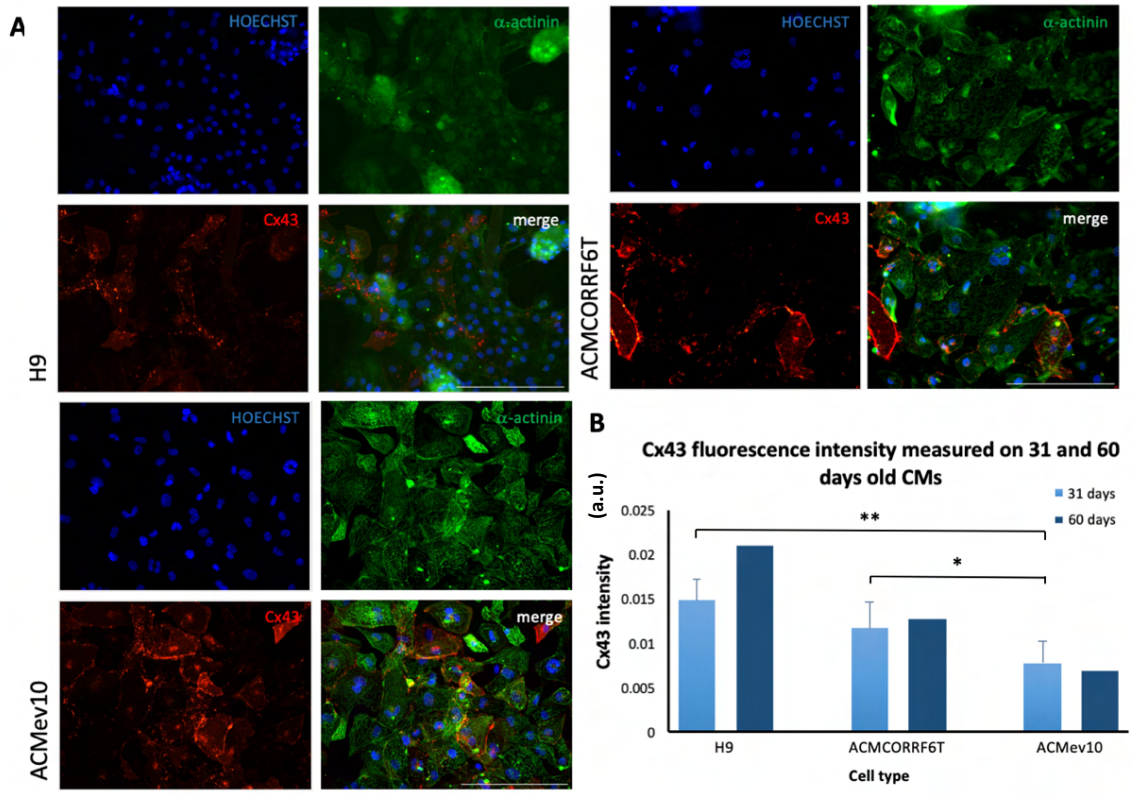

Fig. 17: Induced pluripotent stem cell-derived ACMev10 and H9 cardiomyocytes express α-actinin, Cx43, N-cadherin and lamin A/C. **A:** Immunofluorescence images of 31 days old H9, ACMCORRF6T and ACMev10 cardiomyocytes stained for α-actinin and Cx43. Scalebar 200 µm. **B:** Cx43 fluorescence intensity of 31 and 60 days old cardiomyocytes (*P*<0,0001** between 31 day old ACMev10 and H9; *P*=0,0109* between 31 day old ACMev10 and ACMCORRF6T) (N_{H9} = 603; $N_{ACMCORRF6T}$ = 642; $N_{ACMev10}$ = 386).

Sarcomere lengths in ACMev10 CMs are significantly larger, accompanied by a decrease in α-actinin fluorescence intensity

Confocal imaging of α-actinin-stained CMs revealed loss of sarcomere alignment and organisation in ACMev10 CMs (Fig. 18A). The unpaired t-test revealed that sarcomere lengths of ACMev10 CMs was significantly higher than that of H9 CMs (*P*<0,0001**) (Fig. 18B). Moreover, a high degree of variability and disorganisation was noted in hiPSC-derived ACMev10 CMs, which manifests itself as the high degree of dispersion seen on the violin plot. In addition to the difference observed, the data obtained confirms that the yielded CMs are mature. Analysis of α-actinin intensity revealed an extremely significant difference between H9 and ACMev10 CMs on one hand, and a significant difference between ACMCORRF6T and ACMev10 CMS on the other hand (Fig. 18C).

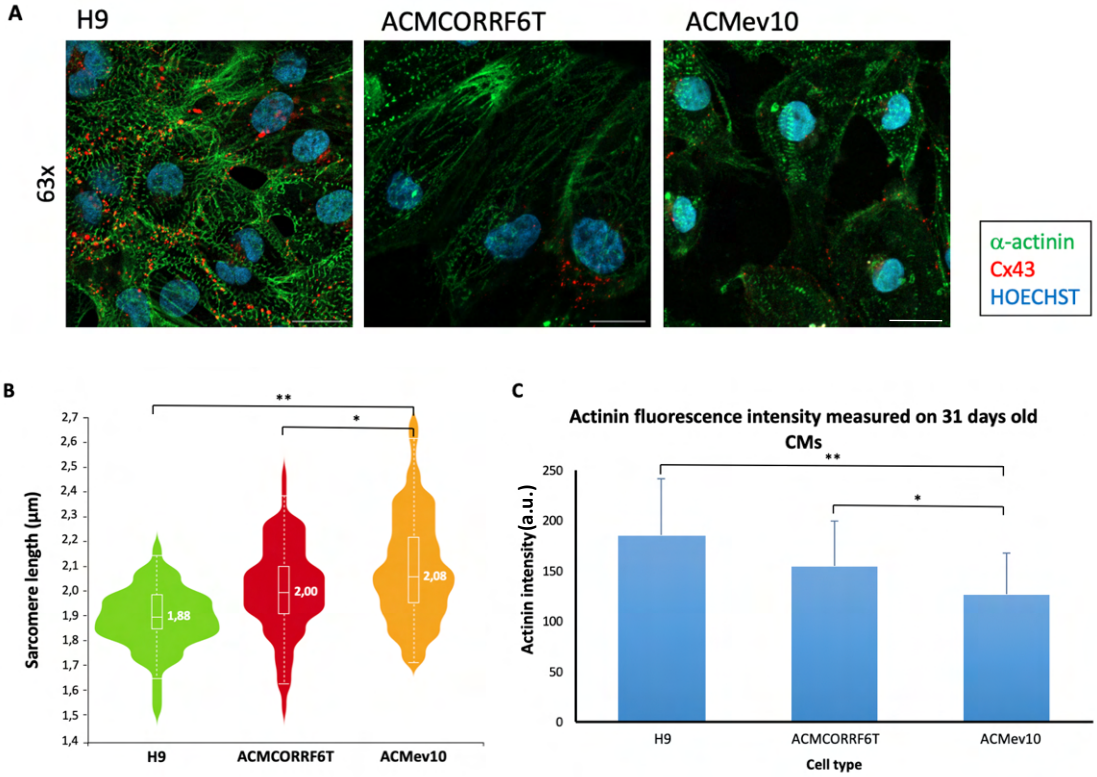

Fig. 18: **A:** Confocal imaging of 31-day old induced pluripotent stem cell-derived H9 and ACMev10 cardiomyocytes stained for α-actinin, Cx32 and HOECHST (63x). Clear loss of sarcomeric organization could be observed on ACMev10 cardiomyocytes, along with a hypertrophic morphology. **B:** Analysis of sarcomere length of induced pluripotent stem cell-derived H9, ACMCORRF6T and ACMev10 cardiomyocytes stained for α-actinin (*P*<0,0001** between ACMev10 and H9; *P*=0,0115* between ACMev10 and ACMCORRF6T) (N_{H9} = 77; $N_{ACMCORRF6T}$ = 70; $N_{ACMev10}$ = 81). **C:** α-actinin fluorescence intensity measured on 31 days old H9, corrected and ACMev10 cardiomyocytes stained for α-actinin (*P*<0,0001**, N_{H9} = 242; $N_{ACMCORRF6T}$ = 242; $N_{ACMev10}$ = 243).

Staining and quantification of plakoglobin reveals nuclear translocation of plakoglobin in ACMev10 CMs

ACMev10 CMs stained for α-actinin and PG exhibited a marked increase in PG fluorescence signal in the nucleus when compared to corrected controls (Fig. 19A-B). Although this could be noted solely by using fluorescence microscopy, a fluorescence intensity analysis was performed to relatively quantify this difference. A significant difference (*P*<0,0001**) was noted between 31 days old ACMev10 and ACMCORRF6T CMs (Fig. 19C). It should be noted that the nuclear plakoglobin in corrected cells is – probably – not zero, however the signal was too low to perform this analysis.

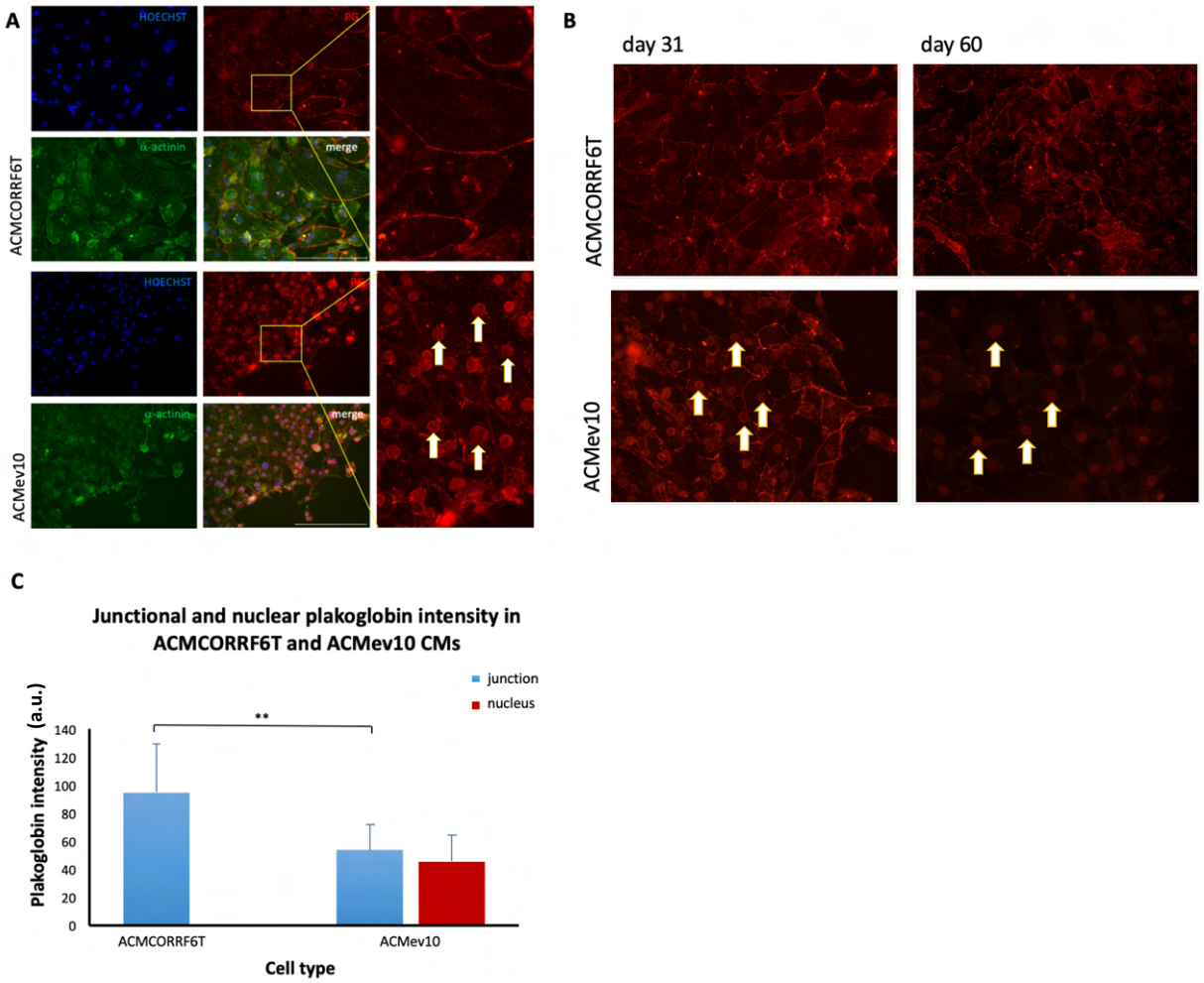

Fig. 19: **A-B:** Induced pluripotent stem cell-derived ACMev10 and ACMCORRF6T cardiomyocytes express α-actinin and plakoglobin (PG). Nuclear translocation of PG can be seen on ACMev10 cardiomyocytes (white arrows) whereas this is not the case for corrected cardiomyocytes. Scalebar 200 µm. **C:** Relative expression of plakoglobin at the junction vs. in the nucleus in 31 days old ACMev10 and ACMCORRF6T cardiomyocytes (*P*<0,0001**) ($N_{ACMCORRF6T}$ = 90; $N_{ACMev10}$ = 76).

MEA analysis shows clustering and higher beating period irregularity in ACMev10 CMs compared to CRISPR-Cas9 corrected and H9 embryonic controls

A total of around 30 000 CMs were seeded onto electrode-containing MEA plates and recorded over a period of 3 minutes. A total of 3 wells with each 16 electrodes was tested per line. Waveforms represent data measured one a signle electrode over the course of 1 minute. Plotting of beat period irregularity showed a markedly higher irregularity in ACMev10 compared to corrected controls (27,58% compared to 3,24%). Clustering of contractions was observed in ACMev10 CMs with shorter prolonged beating intervals (Fig. 20A).

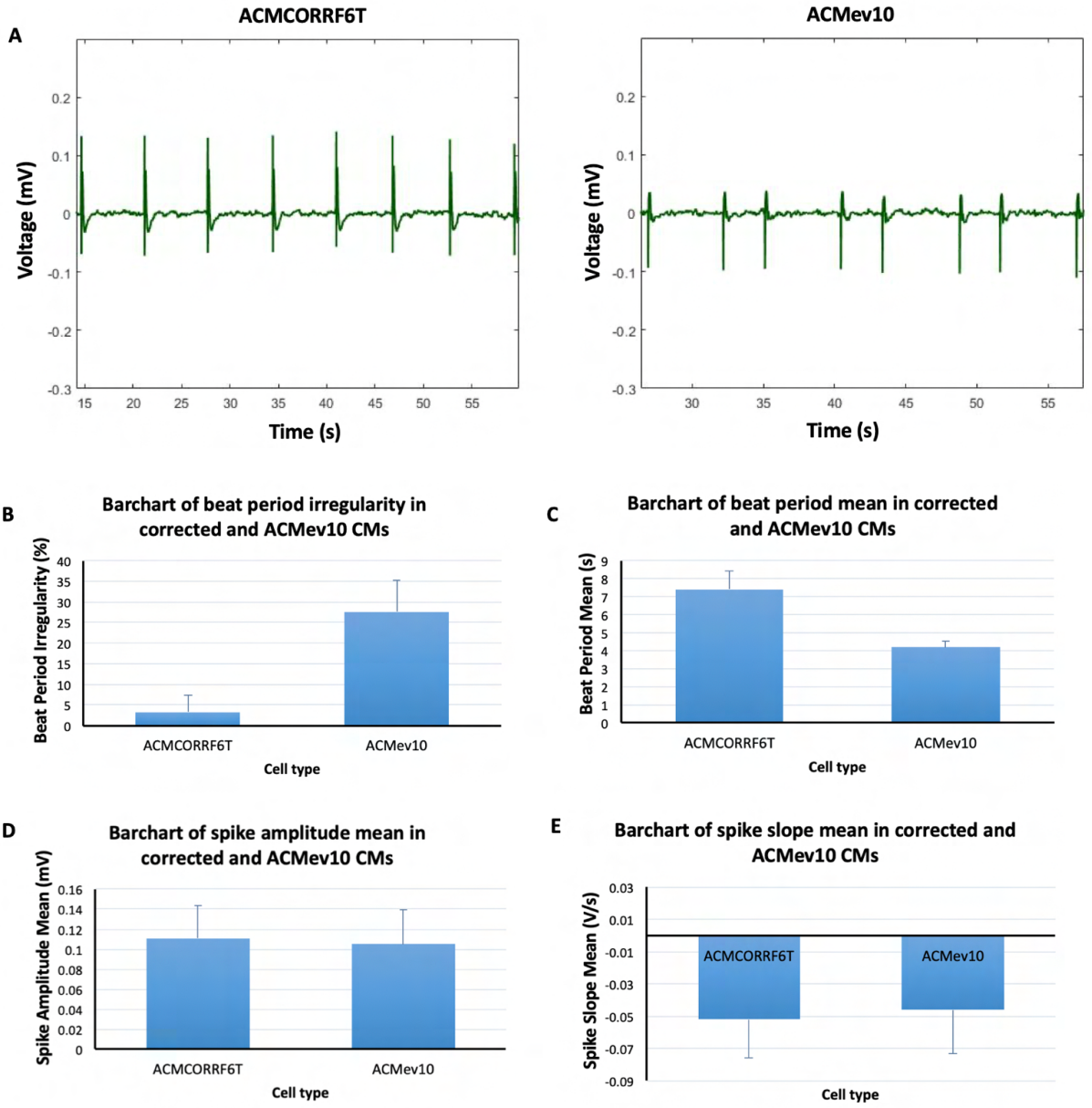

Fig. 20: MEA analysis results of 31 days old ACMCORRF6T (7 active wells) and ACMev10 (8 active wells) CMs. **A:** Waveforms showing voltages (mV) measured over a period of 60 seconds in ACMCORRF6T CMs (left) and ACMev10 CMs (right). **B-E:** Barcharts of beat period irregularity (%)(**B**), beat period mean (s)(**C**), spike amplitude mean (mV)(**D**) and spike slope mean (V/s)(**E**) of ACMCORRF6T and ACMev10 CMs.

6. Discussion

Arrhythmogenic cardiomyopathy is a congenital heart disease characterized by repeated arrhythmias that can potentially be fatal and touches rather young patients. However, even though tools exist to study symptomatic aspect of the disease such as the electrocardiogram, little is known about the pathology's early development mechanisms. This lack of understanding can be tackled by studying patient-specific induced pluripotent stem cells, which are obtained via a non-invasive way and carry all the genetic information of the patient. Therefore, we used the iPSC technology to study cardiomyocytes obtained from two ACM patients as well as an H9 embryonic control and a CRISPR-Cas9 corrected control.

To ensure the reliability of our corrected CMs, it is crucial to also ensure the safety and good working of our CRISPR-corrected stem cells. Towards this end, a pluripotency staining was performed for markers SOX2, NANOG and OCT3/4 on stem cells corrected using the genome editing CRISPR-Cas9 tool. As previously mentioned, two corrected clones were obtained, from which one was corrected using a repair template for *DSP* (ACMCORRF6T), and the other was corrected via homology directed repair using the correct *DSP* allele from the cell's own genome (ACMCORRF1-T). The ACMCORRF1-T was thus used as a control for the stem cells corrected using a repair template, i.e. to assure the efficacy of the repair template. Our results demonstrated that stem cells corrected with genome editing tool CRISPR-Cas9 maintained their pluripotency. Both OCT3/4 antibodies were efficient but seemed to only penetrate into the border of the cell pellet and not in the centre. We could thus conclude that both stem cells corrected without and with repair template were successfully reprogrammed towards pluripotent stem cells, and that the use of CRISPR-Cas9 did not affect the pluripotency of the cells. Therefore, the stability and reliability of the used stem cells was guaranteed. A second tool used to demonstrate the stem cells' pluripotency was trilineage differentiation capacity. Indeed, a stem cell is characterized by its ability to differentiate into tissues that contribute to the three embryonic germ layers, i.e. the endoderm, mesoderm and ectoderm. For both iPSC cell lines, populations were selected for differentiation and compared to the iPSC. The trilineage differentiation of ACMdv4, ACMev10 and corrected samples showed physiological morphology of ectodermal, mesodermal and endodermal cells. Gene analysis using RT-qPCR was performed on 2 technical replicates but 1 biological replicate for ACMdv4 and corrected cells. The genetic upregulation is an indicator of differentiation towards the germ lines. Taken together, this data suggests that our iPSCs are pluripotent and able to differentiate into cells constituting all three germ layers.

Once the pluripotency and reliability of our stem cells was proved, differentiation could be started. Two separate protocols were used towards this end, i.e. the protocol routinely used in our laboratory that is a modified version of Burridge and colleagues' protocol [41], as well as *Maas et al.*'s cardiomyocyte expansion protocol. This last protocol was tested with the wish to multiply our number of CMs. Trial of the expansion protocol by *Maas* and colleagues did not prove successful. Specifically, after replating ACMev10 CMs using CHIR99021, the cells began showing signs of stress. These included the formation of extracellular droplets, intracellular vacuoles and multinucleation. Possibly, this aberrant morphology could be attributed to the use of CHIR99021 on mature CMs. However, this phenotype was not noticed when culturing H9 cells with this protocol. We speculate that the extracellular vesicles seen after replating of ACMev10 CMs could be fat droplets, seen the adipogenic nature of ACM [13]. Additionally, hurdles were encountered in the differentiation of the ACMdv4 hiPSC-derived cell line. Unfortunately, we were unable to carry the cells past day 4 of the differentiation protocol. We therefore hypothesized that the ACMdv4 cells were susceptible to IWP2 – the small molecule used to supplement cardio differentiation medium with on day 4. The cell population systematically detached from the culturing plate. No changes were observed by trying out of different batch of IWP2. Possibly, the cell population in the thawed vial was suboptimal, for example due to prolonged contact with cytotoxic cryoprotectant DMSO.

After differentiation of the iPSCs towards CMs, their morphology was assessed. This was done by means of phase-contrast microscopy, fluorescence microscopy and confocal microscopy. To visualize the cells with fluorescence and confocal microscopy and distinguish Cx43 or PG expression, a staining first needed to be performed. Markers chosen for this staining included TNNT2 and NKX2.5, which are indicative of a CM identification. Analysis of NKX2.5 and HOECHST colocalization exhibited a high percentage of CM status (>80% [25]), which supports the efficacy of our differentiation protocol. From here on, we focussed on finding disease-specific markers or morphological changes for ACM. Indications have been provided by *Shah* and colleagues that the circularity of the CMs' nuclei is affected in their model for hypertrophic cardiomyopathy, which employs a human cell line carrying a mutation in LMNA (lamin A/C) [50]. They observed a decrease in nuclear circularity in the aberrant cells. We therefore sought to look at the nuclear circularity of our CMs by analysing both HOECHST and lamin A/C-stained cells. The student's T-test detected a significant difference in nuclear circularity of HOECHST-stained nuclei between H9/ACMev10 and corrected/ACMev10 cells, with the nuclei of ACMev10 CMs being significantly smaller than the controls. These differences are however probably not biologically relevant seen the minute difference between sample medians.

Because our study focuses on ACM with pathogenic variants in *DSP*, and that the DSP protein is tightly linked to desmin intermediate filaments that signal to the nucleus, we decided to take a further look at the effects of *DSP* mutations on the nuclear lamina. Lamin A/C proteins form a dense network of intermediate filaments that are not specific to CMs, but can be found in most differentiated somatic cells. Lamin A/C polymers are crucial in the formation of the nuclear lamina or envelope, thereby safeguarding the integrity of the nucleus. Other roles of the protein include communication with cellular proteins, organisation of intranuclear chromatin and regulation of mechanotransduction [4]. In an CM model for ACM carrying a nonsense (truncating) *LMNA* mutation, *De Zio et al.* demonstrated differences in lamin expression between control and ACM samples [4]. While in control samples a clearly defined envelope could be observed by means of immunofluorescence, the signal was found to be more diffused in affected CMs [4]. Nuclear lamin accumulated in the nucleoplasm and formed aggregates at the level of the envelope [4], suggesting a clear difference in phenotype between the two conditions. This trend was also seen in the study conducted by *Shah et al.* on CMs from dilated cardiomyopathy patients (DCM) [50]. CMs derived from DCM patients expressed more nucleoplasmic lamin A compared to control.
We found some evidence of abnormalities in the nuclear lamina as well as apparent folds present in the nucleoplasm. This was however observed in all tested cell lines and is therefore more likely to be due the staining procedure (permeabilization, application of mechanical forces and shear stress, multiple washing steps), or due to the fact that a nucleus is a 3D structure and that our microscopy tool used visualises the cells in 2D.

Furthermore, several studies have found proof of aberrant localization and downregulation of Cx43 and PG in models for ACM. For example, studies such as the ones conducted by *Borrego* and *Gomes* have found evidence of an altered distribution and downregulation of Cx43 and PG in *DSP*-mutant CMs [6, 9]. The group of *Zhang* et al. observed the presence of Cx43 in the intracellular space [22]. We thus performed immunofluorescence staining on CMs for Cx43 and PG, along with α-actinin or TNNT2. The cell populations used were each time 31 days old, a timing at which a more mature phenotype is expected, to allow for comparison.

As Cx43 is a gap junction protein, expression at the cellular border was expected and confirmed through immunofluorescence microscopy [5]. Analysis of Cx43 fluorescence intensity showed a marked reduction in Cx43 fluorescence intensity in 31 days old ACMev10 CMS when compared to H9 and corrected controls. This result is in line with previously reported data. To assess whether CM maturity and age played a role in this intensity, the same analysis was performed on 60 days old CMs. However, as we were only able to produce one batch of these cells, it is not possible to look at any statistical difference between 31 and 60

days old cells. Based off the data we did yield, we could speculate that – seen how Cx43 intensity is slightly increased in 60 days old H9 and corrected CMs – our control cell lines continue to produce Cx43 as they mature until they reach a plateau stage. This increase was not observed in ACMev10 CMs, where a small decrease can even be seen. We thus suggest that *DSP*-mutated CMs yield a lower Cx43 fluorescence intensity compared to non-*DSP*-mutant controls. This difference is probably exacerbated as the CMs grow older and become more mature. Moreover, we did not observe the presence of Cx43 in the intracellular space as was observed by the group of *Zhang* [22].

hiPSC-derived CMs for ACMev10 and CRISPR-corrected cells were stained for PG to investigate the nuclear presence of PG in *DSP*-mutant cells (ACMev10), and cells carrying the correct *DSP* gene (ACMCORRF6T). Clear translocation of PG to the nucleus was observed in ACMev10 CMs under fluorescent microscopy. This was however not the case in ACMCORRF6T cells, showing a restoration of normal PG localisation in CMs that are not defect for *DSP*. As mentioned under paragraph 1c, PG acts as a β1-catenin paralogue and inhibits the transcriptional activity of β1-catenin, whilst also promoting its degradation. Nuclear translocation of PG is thought to negatively affect the Wnt-pathway due to increased β1-catenin degradation [6, 9]. Moreover, a fluorescence intensity analysis was performed to investigate the relative presence of PG at the junction and compare it to nuclear PG. This analysis revealed an almost 2-fold decrease of junctional PG in ACMev10 CMs when compared to the corrected control [5, 13]. An extremely significant difference was observed between the PG at the junction between ACMev10 and ACMCORRF6T CMs, although it should be mentioned this analysis was performed on one biological replicate only. Effects of Wnt-downregulation have been suggested to give rise to the adipogenic character of ACM CMs. Moreover, seen as the canonical Wnt-pathway promotes differentiation when stimulated (Wnt-ON), it is possible that translocation of PG to the nucleus influences CM differentiation, proliferation and maturity by promoting the Wnt-OFF state [5, 13]. The question remains when this translocation happens during differentiation. This could be tested by looking at PG translocation right after applying CHIR99021 and comparing it to translocation right after supplying the cells with IWP2, seen the biphasic Wnt-modulation that results from using these small molecules. We could however not observe any deviances during the differentiation of ACMev10 stem cells to CMs, but it should not be forgotten that an *in vitro* model – manipulated from the outside with small molecules – is not fully representative of the situation *in vivo*.

Actinin stainings were used to assess the sarcomere length of our CMs, as sarcomere length is a good indicator of CM maturity. Indeed, decrease in length has already been observed in a model for hypertrophic cardiomyopathy [27]. The physiological length of a sarcomere unit in man has been established at 2,2 µm, with a high degree of organisation [25]. Sarcomere length analysis revealed a markedly increased sarcomere length in ACMev10 CMs as opposed to H9 and corrected controls. Interestingly and against our expectation, we found that the average length in ACMev10 CMs comprised 2,08 µm, while the average sarcomere length of H9 controls equals 1,88 µm. Loss of sarcomeric organisation manifested itself as a high degree of dispersion on the violin plots and could also be observed visually. It is possible that culturing of CMs on a rigid 2D surface enhances the stretch of the cells and influences the sarcomere length. Moreover, lengths were measured manually, which – although following the principle of distance between intensity peaks as used in other studies – might affect the obtained data. Additionally, study of sarcomere length further supports the maturity of our in vitro model, with average lengths being not far removed from the physiological 2,2 µm observed in healthy human cardiac tissue [23, 25]. As for α-actinin fluorescence intensity, no indications of a reduced expression nor intensity of the protein have been suggested in current models for ACM. In their zebrafish model, *Ma* and colleagues did not note a difference in α-actinin fluorescence intensity between their control and ARVC line [35]. In an iPSC model for hypertrophic cardiomyopathy with a pathogenic variant in *ACTN* itself, no changes in protein expression were identified compared to controls [51].There is at the moment no indication of

a lowered α-actinin expression in ACM. However, decreased expression of actin – the anchoring protein of α-actinin, by 90%, has been suggested in cells that undergo adipogenic differentiation [13]. We measured α-actinin fluorescence intensity on 31 days old CMs and found a significant decrease in intensity in ACMev10 CMs compared to controls. Our obtained results are however attributable to a low sample size and the lack of replicates.

Lastly, we took a look at electrophysiological properties of our cells to investigate the arrhythmogenic tendencies of ACMev10 CMs. This was done by using a multi electrode array test in which a total of 30 000 CMs were seeded per well of a MEA-plate, which contains 16 electrodes in each well. These electrodes allow to measure the field potential per well and each measurement was taken over a course of 3 minutes. *DSP*-mutant CMs contracted with higher beating irregularity than CRISPR-corrected controls. Contraction of ACMev10 CMs manifested itself in clusters with a shorter within-cluster beating period and a prolonged beating time before the next cluster of spikes. Moreover, contraction amplitude of ACMev10 CMs seemed lower on the waveforms, but comparison of spike amplitude mean did not detect any difference. Spike slope means were generally the same across both cell lines, however a small difference existed in ACMev10 CMs, which can be indicative of a possible abberrant phenotype.

7. Conclusion

Overall, this study suggests the presence of abnormalities in *DSP*-mutant hiPSC-derived CMs when compared to H9 and CRISPR-Cas9 corrected controls. *DSP*-mutant CMs exhibited a marked decrease in Cx43, PG and α-actinin fluorescence intensities, along with an increase in sarcomere length. Aberrant localisation of PG in the nucleoplasm of mature *DSP*-mutant CMs was expected and confirmed. Taken together, our data suggests the presence of interaction between DSP and PG at the cellular junction as well as a dysregulation of the Wnt-pathway. CMs produced from ACMdv4 and ACMev10 hiPSC demonstrate specific characteristics that cannot be found in H9 and corrected controls. Importantly, indications were found of an arrhythmogenic tendency in ACMev10 CMs with lowered contraction amplitude and increased beat period irregularity. Limitations of this study include the lack of replicates and/or small sample sizes. As a future perspective, we would want to perform western blotting and RT-qPCR for PG and Cx43. Moreover, the creation of a 3D EHT model would be a noble addition to the experiments performed.

8. References

1. Austin KM, Trembley MA, Chandler SF, Sanders SP, Saffitz JE, Abrams DJ, et al. Molecular mechanisms of arrhythmogenic cardiomyopathy. Nat Rev Cardiol. 2019;16(9):519-37. doi: 10.1038/s41569-019-0200-7. PubMed PMID: 31028357; PubMed Central PMCID: PMCPMC6871180.
2. Calore M, Lorenzon A, De Bortoli M, Poloni G, Rampazzo A. Arrhythmogenic cardiomyopathy: a disease of intercalated discs. Cell Tissue Res. 2015;360(3):491-500. Epub 20141026. doi: 10.1007/s00441-014-2015-5. PubMed PMID: 25344329.
3. Rampazzo A. Genetic bases of arrhythmogenic right ventricular Cardiomyopathy. Heart Int. 2006;2(1):17. Epub 20060528. doi: 10.4081/hi.2006.17. PubMed PMID: 21977247; PubMed Central PMCID: PMCPMC3184660.
4. De Zio R, Pietrafesa G, Milano S, Procino G, Bramerio M, Pepe M, et al. Role of Nuclear Lamin A/C in the Regulation of Nav1.5 Channel and Microtubules: Lesson From the Pathogenic Lamin A/C Variant Q517X. Front Cell Dev Biol. 2022;10:918760. Epub 20220629. doi: 10.3389/fcell.2022.918760. PubMed PMID: 35846372; PubMed Central PMCID: PMCPMC9277463.
5. Rampazzo A, Calore M, van Hengel J, van Roy F. Intercalated discs and arrhythmogenic cardiomyopathy. Circ Cardiovasc Genet. 2014;7(6):930-40. doi: 10.1161/CIRCGENETICS.114.000645. PubMed PMID: 25516623.
6. Cabrera-Borrego E, Montero-Vilchez T, Bermúdez-Jiménez FJ, Tercedor-Sánchez J, Tercedor-Sánchez L, Sánchez-Díaz M, et al. Heterozygous Arrhythmogenic Cardiomyopathy-. J Clin Med. 2021;10(19). Epub 20211008. doi: 10.3390/jcm10194608. PubMed PMID: 34640625; PubMed Central PMCID: PMCPMC8509745.
7. Giacomelli E, Meraviglia V, Campostrini G, Cochrane A, Cao X, van Helden RWJ, et al. Human-iPSC-Derived Cardiac Stromal Cells Enhance Maturation in 3D Cardiac Microtissues and Reveal Non-cardiomyocyte Contributions to Heart Disease. Cell Stem Cell. 2020;26(6):862-79.e11. Epub 20200526. doi: 10.1016/j.stem.2020.05.004. PubMed PMID: 32459996; PubMed Central PMCID: PMCPMC7284308.
8. Stevens TL, Manring HR, Wallace MJ, Argall A, Dew T, Papaioannou P, et al. Humanized. Cells. 2022;11(19). Epub 20220929. doi: 10.3390/cells11193049. PubMed PMID: 36231013; PubMed Central PMCID: PMCPMC9562631.
9. Gomes J, Finlay M, Ahmed AK, Ciaccio EJ, Asimaki A, Saffitz JE, et al. Electrophysiological abnormalities precede overt structural changes in arrhythmogenic right ventricular cardiomyopathy due to mutations in desmoplakin-A combined murine and human study. Eur Heart J. 2012;33(15):1942-53. Epub 20120111. doi: 10.1093/eurheartj/ehr472. PubMed PMID: 22240500; PubMed Central PMCID: PMCPMC3409421.
10. Smith ED, Lakdawala NK, Papoutsidakis N, Aubert G, Mazzanti A, McCanta AC, et al. Desmoplakin Cardiomyopathy, a Fibrotic and Inflammatory Form of Cardiomyopathy Distinct From Typical Dilated or Arrhythmogenic Right Ventricular Cardiomyopathy. Circulation. 2020;141(23):1872-84. Epub 20200506. doi: 10.1161/CIRCULATIONAHA.119.044934. PubMed PMID: 32372669; PubMed Central PMCID: PMCPMC7286080.
11. Adams JN, Brooks M, Redpath TW, Smith FW, Dean J, Gray J, et al. Aortic distensibility and stiffness index measured by magnetic resonance imaging in patients with Marfan's syndrome. Br Heart J. 1995;73(3):265-9. doi: 10.1136/hrt.73.3.265. PubMed PMID: 7727188; PubMed Central PMCID: PMCPMC483810.

12. Shiba M, Higo S, Kondo T, Li J, Liu L, Ikeda Y, et al. Phenotypic recapitulation and correction of desmoglein-2-deficient cardiomyopathy using human-induced pluripotent stem cell-derived cardiomyocytes. Hum Mol Genet. 2021;30(15):1384-97. doi: 10.1093/hmg/ddab127. PubMed PMID: 33949662; PubMed Central PMCID: PMCPMC8283207.
13. Garcia-Gras E, Lombardi R, Giocondo MJ, Willerson JT, Schneider MD, Khoury DS, et al. Suppression of canonical Wnt/beta-catenin signaling by nuclear plakoglobin recapitulates phenotype of arrhythmogenic right ventricular cardiomyopathy. J Clin Invest. 2006;116(7):2012-21. doi: 10.1172/JCI27751. PubMed PMID: 16823493; PubMed Central PMCID: PMCPMC1483165.
14. Kleber AG, Saffitz JE. Role of the intercalated disc in cardiac propagation and arrhythmogenesis. Front Physiol. 2014;5:404. Epub 20141017. doi: 10.3389/fphys.2014.00404. PubMed PMID: 25368581; PubMed Central PMCID: PMCPMC4201087.
15. van Kampen SJ, Han SJ, van Ham WB, Kyriakopoulou E, Stouthart EW, Goversen B, et al. PITX2 induction leads to impaired cardiomyocyte function in arrhythmogenic cardiomyopathy. Stem Cell Reports. 2023. Epub 20230213. doi: 10.1016/j.stemcr.2023.01.015. PubMed PMID: 36868229.
16. Sikora M, Ermel UH, Seybold A, Kunz M, Calloni G, Reitz J, et al. Desmosome architecture derived from molecular dynamics simulations and cryo-electron tomography. Proc Natl Acad Sci U S A. 2020;117(44):27132-40. Epub 20201016. doi: 10.1073/pnas.2004563117. PubMed PMID: 33067392; PubMed Central PMCID: PMCPMC7959525.
17. Ng R, Manring H, Papoutsidakis N, Albertelli T, Tsai N, See CJ, et al. Patient mutations linked to arrhythmogenic cardiomyopathy enhance calpain-mediated desmoplakin degradation. JCI Insight. 2019;5. Epub 20190613. doi: 10.1172/jci.insight.128643. PubMed PMID: 31194698; PubMed Central PMCID: PMCPMC6675562.
18. Goossens S, Janssens B, Bonné S, De Rycke R, Braet F, van Hengel J, et al. A unique and specific interaction between alphaT-catenin and plakophilin-2 in the area composita, the mixed-type junctional structure of cardiac intercalated discs. J Cell Sci. 2007;120(Pt 12):2126-36. Epub 20070529. doi: 10.1242/jcs.004713. PubMed PMID: 17535849.
19. Zhurinsky J, Shtutman M, Ben-Ze'ev A. Plakoglobin and beta-catenin: protein interactions, regulation and biological roles. J Cell Sci. 2000;113 (Pt 18):3127-39. doi: 10.1242/jcs.113.18.3127. PubMed PMID: 10954412.
20. Gutstein DE, Morley GE, Tamaddon H, Vaidya D, Schneider MD, Chen J, et al. Conduction slowing and sudden arrhythmic death in mice with cardiac-restricted inactivation of connexin43. Circ Res. 2001;88(3):333-9. doi: 10.1161/01.res.88.3.333. PubMed PMID: 11179202; PubMed Central PMCID: PMCPMC3630465.
21. Yao JA, Gutstein DE, Liu F, Fishman GI, Wit AL. Cell coupling between ventricular myocyte pairs from connexin43-deficient murine hearts. Circ Res. 2003;93(8):736-43. Epub 20030918. doi: 10.1161/01.RES.0000095977.66660.86. PubMed PMID: 14500334.
22. Zhang Q, Deng C, Rao F, Modi RM, Zhu J, Liu X, et al. Silencing of desmoplakin decreases connexin43/Nav1.5 expression and sodium current in HL-1 cardiomyocytes. Mol Med Rep. 2013;8(3):780-6. Epub 20130718. doi: 10.3892/mmr.2013.1594. PubMed PMID: 23877755.
23. Skorska A, Johann L, Chabanovska O, Vasudevan P, Kussauer S, Hillemanns M, et al. Monitoring the maturation of the sarcomere network: a super-resolution microscopy-based

approach. Cell Mol Life Sci. 2022;79(3):149. Epub 20220223. doi: 10.1007/s00018-022-04196-3. PubMed PMID: 35199227; PubMed Central PMCID: PMCPMC8866374.
24. Martin TG, Kirk JA. Under construction: The dynamic assembly, maintenance, and degradation of the cardiac sarcomere. J Mol Cell Cardiol. 2020;148:89-102. Epub 20200910. doi: 10.1016/j.yjmcc.2020.08.018. PubMed PMID: 32920010; PubMed Central PMCID: PMCPMC7736463.
25. Ronaldson-Bouchard K, Ma SP, Yeager K, Chen T, Song L, Sirabella D, et al. Advanced maturation of human cardiac tissue grown from pluripotent stem cells. Nature. 2018;556(7700):239-43. Epub 20180404. doi: 10.1038/s41586-018-0016-3. PubMed PMID: 29618819; PubMed Central PMCID: PMCPMC5895513.
26. Lemcke H, Skorska A, Lang CI, Johann L, David R. Quantitative Evaluation of the Sarcomere Network of Human hiPSC-Derived Cardiomyocytes Using Single-Molecule Localization Microscopy. Int J Mol Sci. 2020;21(8). Epub 20200417. doi: 10.3390/ijms21082819. PubMed PMID: 32316650; PubMed Central PMCID: PMCPMC7216082.
27. Wu H, Yang H, Rhee JW, Zhang JZ, Lam CK, Sallam K, et al. Modelling diastolic dysfunction in induced pluripotent stem cell-derived cardiomyocytes from hypertrophic cardiomyopathy patients. Eur Heart J. 2019;40(45):3685-95. doi: 10.1093/eurheartj/ehz326. PubMed PMID: 31219556; PubMed Central PMCID: PMCPMC7963137.
28. Wang L, Kim K, Parikh S, Cadar AG, Bersell KR, He H, et al. Hypertrophic cardiomyopathy-linked mutation in troponin T causes myofibrillar disarray and pro-arrhythmic action potential changes in human iPSC cardiomyocytes. J Mol Cell Cardiol. 2018;114:320-7. Epub 20171205. doi: 10.1016/j.yjmcc.2017.12.002. PubMed PMID: 29217433; PubMed Central PMCID: PMCPMC5800960.
29. Varró A, Tomek J, Nagy N, Virág L, Passini E, Rodriguez B, et al. Cardiac transmembrane ion channels and action potentials: cellular physiology and arrhythmogenic behavior. Physiol Rev. 2021;101(3):1083-176. Epub 20201029. doi: 10.1152/physrev.00024.2019. PubMed PMID: 33118864.
30. Klabunde RE. Cardiac electrophysiology: normal and ischemic ionic currents and the ECG. Adv Physiol Educ. 2017;41(1):29-37. doi: 10.1152/advan.00105.2016. PubMed PMID: 28143820.
31. Aalders J, Léger L, Van der Meeren L, Van den Vreken N, Skirtach AG, Sinha S, et al. Effects of fibrillin mutations on the behavior of heart muscle cells in Marfan syndrome. Sci Rep. 2020;10(1):16756. Epub 20201007. doi: 10.1038/s41598-020-73802-w. PubMed PMID: 33028885; PubMed Central PMCID: PMCPMC7542175.
32. Sacchetto C, Vitiello L, de Windt LJ, Rampazzo A, Calore M. Modeling Cardiovascular Diseases with hiPSC-Derived Cardiomyocytes in 2D and 3D Cultures. Int J Mol Sci. 2020;21(9). Epub 20200511. doi: 10.3390/ijms21093404. PubMed PMID: 32403456; PubMed Central PMCID: PMCPMC7246991.
33. Takahashi K, Yamanaka S. Induction of pluripotent stem cells from mouse embryonic and adult fibroblast cultures by defined factors. Cell. 2006;126(4):663-76. Epub 20060810. doi: 10.1016/j.cell.2006.07.024. PubMed PMID: 16904174.
34. Omole AE, Fakoya AOJ. Ten years of progress and promise of induced pluripotent stem cells: historical origins, characteristics, mechanisms, limitations, and potential applications. PeerJ. 2018;6:e4370. Epub 20180511. doi: 10.7717/peerj.4370. PubMed PMID: 29770269; PubMed Central PMCID: PMCPMC5951134.

35. Ma D, Wei H, Lu J, Ho S, Zhang G, Sun X, et al. Generation of patient-specific induced pluripotent stem cell-derived cardiomyocytes as a cellular model of arrhythmogenic right ventricular cardiomyopathy. Eur Heart J. 2013;34(15):1122-33. Epub 20120713. doi: 10.1093/eurheartj/ehs226. PubMed PMID: 22798562.
36. Inoue H, Nakamura S, Higo S, Shiba M, Kohama Y, Kondo T, et al. Modeling reduced contractility and impaired desmosome assembly due to plakophilin-2 deficiency using isogenic iPS cell-derived cardiomyocytes. Stem Cell Reports. 2022;17(2):337-51. Epub 20220120. doi: 10.1016/j.stemcr.2021.12.016. PubMed PMID: 35063130; PubMed Central PMCID: PMCPMC8828557.
37. Gerull B, Kirchner F, Chong JX, Tagoe J, Chandrasekharan K, Strohm O, et al. Homozygous founder mutation in desmocollin-2 (DSC2) causes arrhythmogenic cardiomyopathy in the Hutterite population. Circ Cardiovasc Genet. 2013;6(4):327-36. Epub 20130717. doi: 10.1161/CIRCGENETICS.113.000097. PubMed PMID: 23863954.
38. Hansen A, Eder A, Bönstrup M, Flato M, Mewe M, Schaaf S, et al. Development of a drug screening platform based on engineered heart tissue. Circ Res. 2010;107(1):35-44. Epub 20100506. doi: 10.1161/CIRCRESAHA.109.211458. PubMed PMID: 20448218.
39. Mannhardt I, Breckwoldt K, Letuffe-Brenière D, Schaaf S, Schulz H, Neuber C, et al. Human Engineered Heart Tissue: Analysis of Contractile Force. Stem Cell Reports. 2016;7(1):29-42. Epub 20160519. doi: 10.1016/j.stemcr.2016.04.011. PubMed PMID: 27211213; PubMed Central PMCID: PMCPMC4944531.
40. Bliley JM, Vermeer MCSC, Duffy RM, Batalov I, Kramer D, Tashman JW, et al. Dynamic loading of human engineered heart tissue enhances contractile function and drives a desmosome-linked disease phenotype. Sci Transl Med. 2021;13(603). doi: 10.1126/scitranslmed.abd1817. PubMed PMID: 34290054.
41. Burridge PW, Matsa E, Shukla P, Lin ZC, Churko JM, Ebert AD, et al. Chemically defined generation of human cardiomyocytes. Nat Methods. 2014;11(8):855-60. Epub 20140615. doi: 10.1038/nmeth.2999. PubMed PMID: 24930130; PubMed Central PMCID: PMCPMC4169698.
42. Maas RGC, Lee S, Harakalova M, Snijders Blok CJB, Goodyer WR, Hjortnaes J, et al. Massive expansion and cryopreservation of functional human induced pluripotent stem cell-derived cardiomyocytes. STAR Protoc. 2021;2(1):100334. Epub 20210209. doi: 10.1016/j.xpro.2021.100334. PubMed PMID: 33615277; PubMed Central PMCID: PMCPMC7881265.
43. Johansson H, Simonsson S. Core transcription factors, Oct4, Sox2 and Nanog, individually form complexes with nucleophosmin (Npm1) to control embryonic stem (ES) cell fate determination. Aging (Albany NY). 2010;2(11):815-22. doi: 10.18632/aging.100222. PubMed PMID: 21076177; PubMed Central PMCID: PMCPMC3006024.
44. Friedman JR, Kaestner KH. The Foxa family of transcription factors in development and metabolism. Cell Mol Life Sci. 2006;63(19-20):2317-28. doi: 10.1007/s00018-006-6095-6. PubMed PMID: 16909212.
45. Pauklin S, Vallier L. The Cell-Cycle State of Stem Cells Determines Cell Fate Propensity. Cell. 2014;156(6):1338. Epub 20140313. doi: 10.1016/j.cell.2014.02.044. PubMed PMID: 28898638; PubMed Central PMCID: PMCPMC5652229.
46. Herrmann BG, Labeit S, Poustka A, King TR, Lehrach H. Cloning of the T gene required in mesoderm formation in the mouse. Nature. 1990;343(6259):617-22. doi: 10.1038/343617a0. PubMed PMID: 2154694.

47. Barnes RM, Firulli BA, Conway SJ, Vincentz JW, Firulli AB. Analysis of the Hand1 cell lineage reveals novel contributions to cardiovascular, neural crest, extra-embryonic, and lateral mesoderm derivatives. Dev Dyn. 2010;239(11):3086-97. doi: 10.1002/dvdy.22428. PubMed PMID: 20882677; PubMed Central PMCID: PMCPMC2965316.
48. Davis LK, Meyer KJ, Rudd DS, Librant AL, Epping EA, Sheffield VC, et al. Pax6 3' deletion results in aniridia, autism and mental retardation. Hum Genet. 2008;123(4):371-8. Epub 20080306. doi: 10.1007/s00439-008-0484-x. PubMed PMID: 18322702; PubMed Central PMCID: PMCPMC2719768.
49. Pevny LH, Sockanathan S, Placzek M, Lovell-Badge R. A role for SOX1 in neural determination. Development. 1998;125(10):1967-78. doi: 10.1242/dev.125.10.1967. PubMed PMID: 9550729.
50. Shah D, Virtanen L, Prajapati C, Kiamehr M, Gullmets J, West G, et al. Modeling of. Cells. 2019;8(6). Epub 20190615. doi: 10.3390/cells8060594. PubMed PMID: 31208058; PubMed Central PMCID: PMCPMC6627421.
51. Prondzynski M, Lemoine MD, Zech AT, Horváth A, Di Mauro V, Koivumäki JT, et al. Disease modeling of a mutation in α-actinin 2 guides clinical therapy in hypertrophic cardiomyopathy. EMBO Mol Med. 2022;14(8):e16423. doi: 10.15252/emmm.202216423. PubMed PMID: 35938313; PubMed Central PMCID: PMCPMC9358393.

Poster

FACULTY OF MEDICINE AND HEALTH SCIENCES

CHARACTERISATION OF AN INDUCED PLURIPOTENT STEM CELL LINE FROM AN ARRHYTHMOGENIC CARDIOMYOPATHY PATIENT CARRYING A PATHOGENIC VARIANT IN DESMOPLAKIN

[1]Medical Cell Research Group, Department of Human Structure and Repair, Faculty of Medicine and Health Science, Ghent University, Ghent, Belgium
[2]Department of Molecular Genetics, Faculty of Medicine and Health Science, Maastricht University, Maastricht, The Nederlands
[3]Department of Biology, University of Padova, Padova, Italy

Léa De Bleeckere[1], Laurens Léger[1], Martina Calore[2], Libero Vitiello[3], Alessandra Rampazzo[3], Jolanda van Hengel[1]

Introduction

Arrhythmogenic cardiomyopathy (ACM) is a progressive autosomal dominant disease of the inner cardiac muscle mass with a prevalence of 1:1000 to 1:5000. Clinically, it is defined by fibro-fatty deposits and ventricular arrhythmia potentially increasing the risk of sudden cardiac death with formation of non-contractile scarring tissue. Mutations in desmosomal genes such as in desmoplakin (*DSP*) are causative for the disease, altough molecular mechanisms underlying the disease remain unknown. The desmosome is a macromolecular complex found in the intercalated disc (ID), a junctional structure that connects cardiomyocytes (CMs) longitudinally. Other structures such as adherens junctions, gap junctions and the mixed-type area composita are present in the ID. In this study, induced pluripotent stem cells (iPSC) generated from an ACM patient carrying a pathogenic variant in *DSP* will be differentiated into CMs and compared to a CRISPR-Cas9-generated isogenic line and an independent human embryonic control line.

The aim of this study is to characterize the phenotype of an iPSC-derived CM cell line for this patient as well as for a CRISPR-Cas9 corrected line. Both will be compared to a human embryonic control line.

The desmosome and intercalated disc

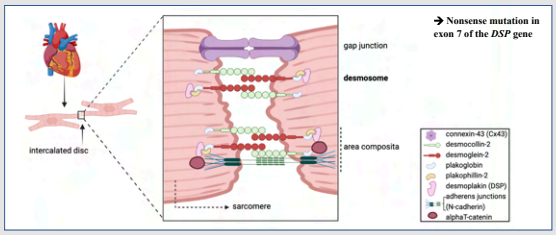

Methodology

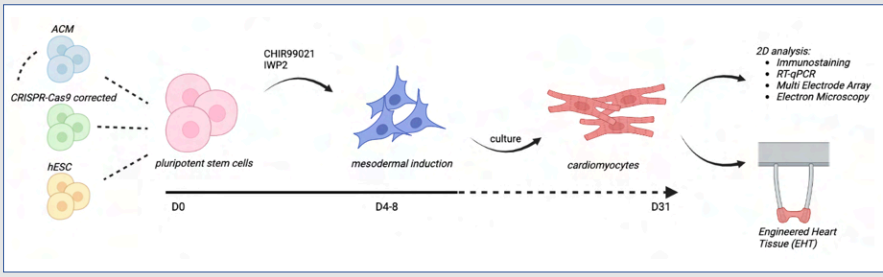

iPSC from different sources can be differentiated towards mature CMs in the span of 31 days. PSC from DSP mutant ACM, CRISPR-Cas9 corrected (isogenic control) and human embryonic stem cells (hESC) will be used. The differentiation will be performed using WNT-pathway regulators CHIR99021 and IWP2, which respectively guide iPSC towards mesoderm and cardiac mesoderm. The obtained CMs will be cultured and analyzed in 2D. Propagation into a fibrin-based Engineered Heart Tissue (EHT) model will be achieved by selecting a pure CM population and casting it in a 3D agarose mold containing silicone poles for auxotonic contraction (Mannhardt, I. et al., 2016).

Results

1. Loss of sarcomere organization and nuclear circularity seen in ACM^{DSPm} CMs

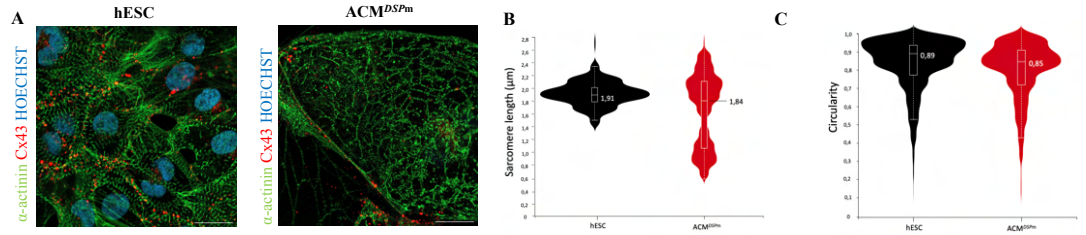

Figure 1: (A) Confocal images of stained hESC and ACM with *DSP* mutation (ACM^{DSPm}) CMs (63x). The sarcomeres are the contractile units of cardiac muscle cells. (B) Combined violin and boxplot of measured sarcomere length. A small, but significant* decrease in sarcomere length was observed in ACM^{DSPm} CMs (1,91 to 1,84 µm) along with clear loss of sarcomeric organization. (C) Combined violin and boxplot of nuclear circularity, measured with ImageJ. Values range from 0 to 1 (perfect circular shape). A small, but significant* decrease was observed between nuclear circularities of hESC and ACM^{DSPm} CMs, meaning the roundness of the nuclei differed between cell lines. This decrease is however not biologically relevant due to the high amount of samples. *$P<0,0001$

2. Fluorescence microscopy shows nuclear translocation of plakoglobin in ACM^{DSPm} CMs

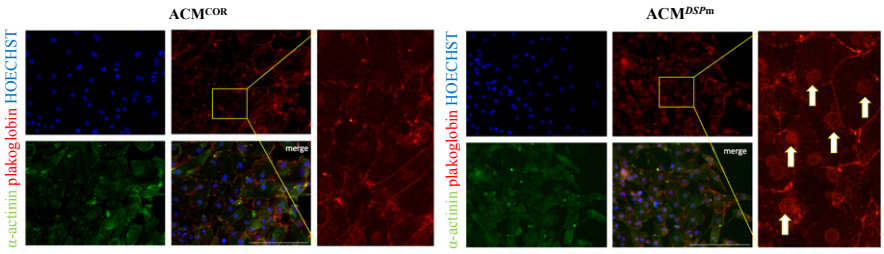

Figure 2: Immunofluorescence images of stained ACM^{DSPm} and corrected (ACM^{COR}) CMs. Scalebar 200 µm. Translocation of plakoglobin signal to the nucleus was observed in ACM^{DSPm} CMs. This can be seen most clearly at the arrows. Plakoglobin is a ß-catenin analog, a protein crucial in the Wnt-pathway for cell survival and differentiation. This pathway is thought to be affected in ACM.

Conclusion

Cardiomyocytes cultured from *DSP*-mutant ACM iPSC show several phenotypical traits that differ from hESC or CRISPR-Cas9 corrected CMs. These differences include loss of sarcomeric organization, a significant decrease in sarcomere length and translocation of palkoglobin to the nucleus. This suggests the unability of ACM-derived CMs to support load and mechanical stress. Nuclear circularity however is not significantly different between control hESC and ACM^{DSPm} CMs. Our findings also support the idea that the Wnt-pathway is deregulated in ACM, as plakoglobin is a ß-catenin analog, a protein crucial in the Wnt-pathway for cell survival and differentiation. This pathway is thought to be affected in ACM.

GHENT UNIVERSITY